JM PAPERS

Angular flow-induced vibrations of a triangular prism

Adrian G. Carleton[1] and Yahya Modarres-Sadeghi[1]

[1]Department of Mechanical and Industrial Engineering, University of Massachusetts, Amherst, MA 01003, USA

Corresponding author: Yahya Modarres-Sadeghi, modarres@engin.umass.edu

We discuss flow-induced vibrations of an equilateral triangular prism confined to travel on a circular path when placed in the concave or convex orientations with respect to the flow. In each orientation, we consider three different initial angles for the prism. In Case 1, one side of the prism sees the flow first; in Case 2, one sharp edge sees the flow first; and in Case 3, one side of the prism is parallel to the incoming flow. We show that the response of the structure as well as the observed wake depend heavily on both the orientation and the initial angle of the prism. Case 1 exhibits vortex-induced vibration (VIV) in the concave orientation and galloping in the convex orientation. Case 2 does not oscillate in the concave orientation; however, oscillates about a mean deflection after a critical reduced velocity in the convex orientation. Case 3 exhibits small-amplitude oscillations in the concave orientation about a mean deflection, while in the convex orientation, exhibits VIV at low reduced velocities, followed by an asymmetric response with VIV features in a half-cycle and galloping features in the other half, and divergence at higher reduced velocities. These different types of responses are accompanied by a myriad of vortex patterns in the wake, from two single vortices shed in the wake in each cycle of oscillations to two vortex pairs, two sets of co-rotating vortices, and a combination of single vortices and vortex pairs depending on the prism's orientation and its initial angle.

Key words: flow-structure interactions, vortex shedding, separated flows

1. Introduction

In flow-induced vibration (FIV), perhaps the most widely studied phenomenon occurs when a flexibly mounted, rigid cylinder is placed in a fluid flow. When the frequency of

vortices shed from the cylinder, which varies with flow velocity, approaches the natural frequency of the cylinder, the fluctuating lift forces on the cylinder cause the onset of large-scale oscillations. When this occurs the vortex shedding becomes synchronised with the motion of the cylinder as the flow velocity is increased. The range of reduced velocities (a dimensionless parameter defined as $U^* = U/(f_n D)$, where U is the incoming flow velocity, f_n is the structure's natural frequency and D is the cylinder's diameter), where oscillations persist and shedding and oscillation frequencies are synchronised, is called the lock-in range. This behaviour is called vortex-induced vibration (VIV) and has been well documented (e.g. Bearman 1984; Blevins 1990; Sarpkaya 2004; Williamson & Govardhan 2004; Vandiver 2012). VIV has also been studied for cases when the degree of freedom is in parallel with the direction of incoming flow, the inline direction (IL VIV) (Cagney & Balabani 2013*a*,*b*; Gurian, Currier & Modarres-Sadeghi 2019), and for cases of two-degrees of freedom flexibly mounted cylinders where oscillations are allowed both in the direction of flow and perpendicular to that (Dahl *et al.* 2007, 2010; Carlson, Currier & Modarres-Sadeghi 2021). In IL VIV and two-dimensional (2-D) VIV also, synchronisations occur between shedding of vortices and oscillation frequency, and lock-in ranges are observed. In general, the maximum amplitude observed in the IL VIV is much smaller than that observed in the CF VIV ($\approx 0.1D$ versus $\approx 1D$), and they are larger in both IL and CF directions in the case of 2-D VIV. It is also shown that one-dimensional (1-D) VIV can be observed when the direction of motion makes an angle with respect to the incoming flow. The VIV response transitions gradually from the typical IL VIV response to the typical CF VIV response as the direction of oscillation transitions from the IL to the CF direction (Benner & Modarres-Sadeghi 2021). As expected, VIV can also be observed in cases where the structure is flexible. There are several studies on VIV of continuous, flexible structures with circular cross-sections (Bourguet *et al.* 2011; Vandiver 2012; Seyed-Aghazadeh & Modarres-Sadeghi 2016; Seyed-Aghazadeh, Edraki & Modarres-Sadeghi 2019), and they show that synchronisation can be observed between shedding frequency and natural frequencies of different modes of the structure, resulting in the excitations of different modes at different reduced velocities or multi-modal response of the structure.

A handful of studies have considered systems where the cylinder is allowed to travel on a curved path, using numerical (Sung *et al.* 2015; Arionfard & Mohammadi 2021; Bourguet 2023), experimental (Arionfard & Nishi 2017) and analytical (Malefaki & Konstantinidis 2020) methods. These studies have been primarily focused on energy harvesting applications, but have noted variations in amplitudes of oscillations and shedding synchronisation depending on the specifics of the curved path. Recently, we also examined the behaviour of a circular cylinder confined to travel on a curved path and placed in fluid flow (Carleton & Modarres-Sadeghi 2024) and showed that the concavity of the path of motion relative to the flow and the radius of curvature of that path have dramatic effects on the VIV response of the system. Convex paths exhibit larger oscillation amplitudes and shorter lock-in ranges with multiple branches, whereas the concave paths have smaller amplitudes and increased lock-in ranges, with no sudden jumps in amplitude of oscillations.

Several studies have considered bluff bodies with non-circular cross-sections placed in flow. In these cases, the angle of attack has a significant effect on the response of the system and, in addition to VIV responses, these systems can exhibit galloping: large-amplitude oscillations that occur at a frequency markedly less than the shedding frequency, where no synchronisation occurs between the structure and vortices. Instead, the observed oscillations are due to a negative flow-induced damping imposed on the structure by the mean flow forces that act on it (Modarres-Sadeghi 2022). Païdoussis *et al.* (2010)

present a comprehensive review of studies on galloping behaviour, which is observed for structures with triangular, rectilinear and D-shaped cross-sections, among others.

Square cross-section prisms are perhaps the most widely studied of these, both experimentally and numerically (Parkinson & Wawzonek 1981; Obasaju, Ermshaus & Naudascher 1990; Naudascher & Wang 1993; Deniz & Staubli 1997; Su *et al.* 2007; Nemes *et al.* 2012; Zhao, Cheng & Zhou 2013; Carlson *et al.* 2021; Gurian & Modarres-Sadeghi 2021; Benner, Carleton & Modarres-Sadeghi 2025), and it has been shown that this system can undergo both VIV and galloping. Parkinson & Smith (1964) observed galloping of a square cross-section with an angle of attack of $\alpha = 0°$, where the sides of the prism are all either parallel or perpendicular to the flow. A later study by Bokaian & Geoola (1984) noted mixed modes of VIV and galloping in the response. Further investigations of this system revealed that the specifics of the response, whether VIV, galloping or both, are highly dependent on the initial angle of attack, with a transition from one to the other occurring over a narrow range of angles of attack due to the sudden change in the separation point (Nemes *et al.* 2012). The shedding patterns for a galloping square prism, with $\alpha = 0°$, were found to exhibit frequencies at integer multiples of the oscillation frequency, whereas multiple wake modes were observed for a VIV-dominated response with $\alpha = 45°$ (Zhao *et al.* 2014*a*). Varying the aspect ratio of a rectilinear prism further breaks the symmetry of the system, and promotes a galloping response over VIV (Cui *et al.* 2015).

There are several studies on triangular prisms fixed in flow or externally forced to oscillate, where the effect of angle of attack and the type of triangle (e.g. equilateral, isosceles) are investigated (Kumar De & Dalal 2006; De & Dalal 2007; Bao, Zhou & Zhao 2010). A numerical study by Tu *et al.* (2014) examined the flow past an equilateral triangular prism, both when static and when forced to oscillate rotationally about its axis, and presented a comprehensive mapping of the wakes developed over all angles of attack and a range of Reynolds numbers. They observed that the separation point varied with the Reynolds number for some angles of attack, and was independent from it for others. They also observed that both 2S shedding patterns (where two single vortices are shed per cycle of oscillations) and P + S shedding patterns (where a pair of vortices and a single vortex are shed during a cycle) were present. Self-excited rotational oscillations of a triangular prism have also been studied for both single prisms (Srigrarom & Koh 2008) and tandem arrangements (Wang *et al.* 2011).

Studies have also been performed on triangular prisms allowed to oscillate in the CF direction, using 2-D numerical simulations (e.g. Alawadhi 2013), wind tunnel experiments with non-equilateral prisms (e.g. Alonso, Meseguer & Pérez-Grande 2005; Alonso & Meseguer 2006) or water tunnel experiments with equilateral prisms (Seyed-Aghazadeh, Carlson & Modarres-Sadeghi 2017). Alonso *et al.* (2005) and Alonso & Meseguer (2006) used a long beam, allowed to pivot at one end, to create a pendulum like path. However, unlike in the present study, in their experimental set-up, the length of the beam was significantly longer than the amplitude of oscillations, such that the oscillations were considered 'quasi-translational' and the variations in angle of attack were negligible. They determined that galloping was influenced by both the angle of attack and the main vertex angle of the prism. Seyed-Aghazadeh *et al.* (2017) examined the CF response of an equilateral triangular prism at all angles of attack, and over a large range of reduced velocities to generate a comprehensive mapping of the structural response and wake characteristics of the system. This study found that no oscillations occur for an equilateral triangular prisms with angles of attack less than $\alpha = 25°$, where $\alpha = 0°$ corresponds to one edge of the prism facing directly upstream. At greater α values, both isolated VIV and galloping regimes, and VIV directly transitioning to galloping regimes were observed.

Additionally, a variety of shedding patterns were noted, changing with both the angle of attack and the reduced velocity.

Flow-induced vibrations of a prism with a triangular cross-section have been noted as representative of a variety of real-world conditions (Zhu *et al.* 2019; Jafari, Hou & Abdelkefi 2020) wherein material either accumulates on a structure (such as ice-buildup) or the structure erodes or corrodes away (such as in submerged structures). While the initial design of a structure might use symmetric bluff bodies and account for the expected FIV behaviour associated with those, as the geometry of the structure changes, a variety of new behaviours can arise that could be sensitive to the specific way in which the symmetry of the bluff body is broken. Additionally, while the canonical FIV systems are often studied for purely translation degrees of freedom, real-world applications are often more complex. Long, thin structures in flow, such as mooring lines and power transmission lines, exhibit a downstream deflection in addition to oscillations, and the resultant path of motion is often a concave arc. Cantilevered structures also follow curved paths when oscillating.

There are also potential applications in renewable energy harvesting. Many recent studies have explored energy harvesters that use VIV or galloping to generate energy (Bernitsas *et al.* 2008; Ma & Zhou 2022; Edraki, Benner & Modarres-Sadeghi 2023). These past studies have shown that galloping could be more efficient than VIV for extracting energy (Barrero-Gil, Alonso & Sanz-Andres 2010), since inherently larger amplitudes of oscillations are expected in a galloping system than a system that undergoes VIV, and also since there is theoretically no upper limit for flow velocities that could cause galloping in a system, while VIV is expected to occur only over a range of flow velocities. These potential applications could benefit from a better understanding of the behaviour of non-circular structures that could potentially undergo galloping on curved paths, especially since in many of these energy harvesters, the bluff body is attached to the tip of a cantilevered beam and oscillates on a curved path.

The present study considers the angular flow-induced vibrations of an equilateral triangular prism allowed to move along a curved path, such that the angle it makes with the incoming flow changes continuously throughout its oscillations. This configuration enables the structure to oscillate in both the CF and IL directions while still being a one-degree of freedom (1-DOF) system. Therefore, we can investigate the combined influence of fluctuating lift and drag forces that act on the structure on the resulting motion. The questions that arise are whether or not we observe VIV and galloping in such systems as well, similar to what we normally observe in a system allowed to oscillate on a straight line. Additionally, if we observe VIV and galloping, do they have the same features as those observed in cases with oscillations on a straight line or do we observe new features?

2. Experimental set-up

The experiments were conducted in a 50 cm × 38 cm × 127 cm test-section of a water tunnel capable of flow velocities from $1 \, \text{cm s}^{-1}$ up to $1 \, \text{m s}^{-1}$, with a uniform flow profile and a turbulence intensity of approximately 2 %. The rotating component of the set-up consisted of an acrylic prism with a length of $L = 25.4$ cm and an equilateral triangular cross-section with a side length of $S = 2.54$ cm. At each end of this prism, two threaded holes were machined along a line passing through the centroid of the cross-section, with the axes of all four holes being co-planar. One prism was made such that the holes were on a line passing from one edge to the midpoint of the opposite side (for Cases 1 and 2 in figure 1) and a second prism was made with the holes on a line parallel to one edge of the prism for Case 3. The holes were used to attach 6.5 mm thick circular acrylic plates to each end of the prism and, by using a pair of screws, any possible rotation between the
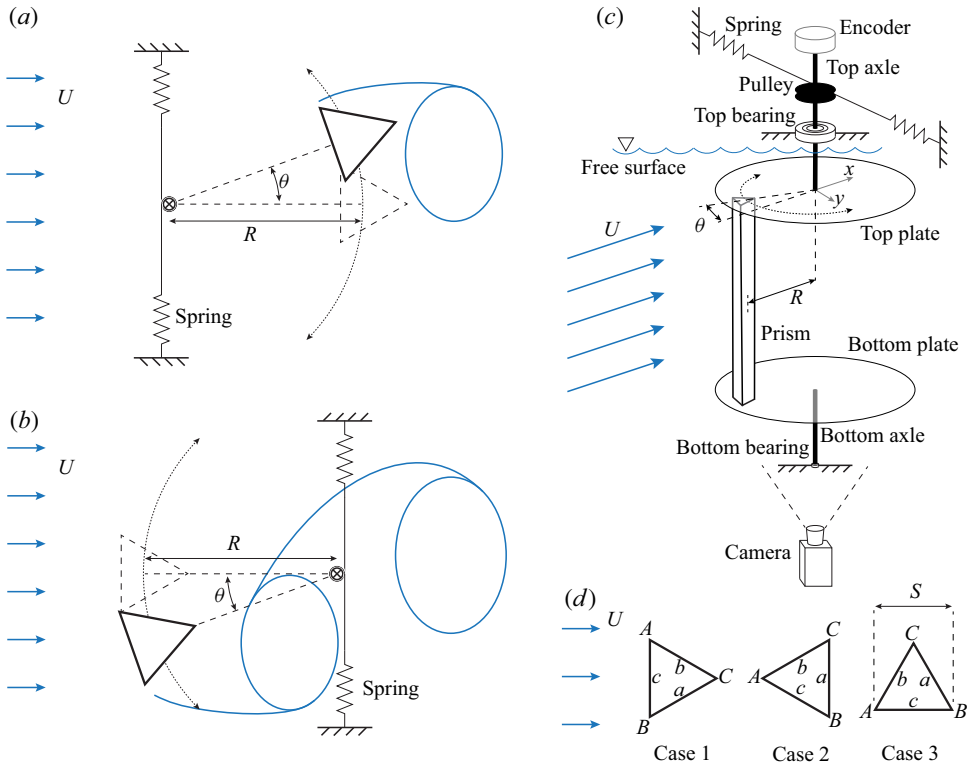
Figure 1. A schematic of the experimental set-up showing (*a*) the path of motion of the prism in a horizontal plane for Case 1 in the concave orientation and (*b*) Case 1 in the convex orientation. (*c*) A 3-D projection of the set-up (for Case 1 in the convex orientation) illustrating the location of important components (note that the rigid framework to which the bearings and springs were mounted is omitted for clarity, and represented by the fixed connection symbols), and (*d*) the three initial orientations tested, shown here when $\theta = 0$. The annotations shown in panel (*d*) will be used later to refer to specific edges (*A*, *B* and *C*), and sides (*a*, *b* and *c*) of the prism.

prism and plates was eliminated. The prism was mounted at an offset of $R = 1.75S$ from the centre of the plates to the geometric enter of the prism – a distance corresponding to the maximum oscillation amplitude observed by the authors during previous experiments using a similar set-up with a circular cylinder (Carleton & Modarres-Sadeghi 2024). Flat-head screws were used for the attachment and the plates were appropriately countersunk so the fasteners would not protrude into the free stream flow. Two axle shafts, made of 9.5 mm diameter aluminium, were mounted to the centre of the plates, on the opposite side as the prism. The wake produced by the axles was separated from the prism by the plates and there was no interaction between the two.

The axles were mounted in bearings at the top and bottom that were connected through a rigid rectangular frame made of 6.5 mm thick clear acrylic sheets that sat flush against the walls of the test section. On the top section of the frame, which sat on the top rails of the test-section above the water line, a bearing block was mounted to hold the top axle, to which a rotary encoder and spring system were attached. Using a Simulink Real-Time Model, the encoder output was recorded and synchronised with high-speed video recorded using a Phantom Miro M110. The spring system consisted of a pulley attached to the top axle, around which a full revolution of mono-filament line was wrapped, which was attached to a matched pair of extensional coil springs, one at each end of the line.

The other ends of the springs were attached to the frame such that there was a straight line between the spring mounting points that was tangential to the surface of the pulley. This configuration balanced the radial forces acting on the axle to prevent binding and created a linear relationship between angular displacement and restoring torque of 0.45 N mm/°. At the opposite end of the rotating assembly, the lower bearing was sized so that its outer diameter matched the outer diameter of the bottom axle, which was turned down at the end to fit the bearing inner diameter, and was held in a recess machined directly into the bottom sheet. Since this bearing was continuously submerged, it was made from corrosion-resistant materials so that it would not become a source of friction. Minimising the size of the bearing and mounting it directly into the acrylic of the frame reduced the visual obstruction of the flow from below, allowing for better flow visualisation. Particle image velocimetry (PIV) was performed by seeding the water tunnel with 50 micron polyamid particles, which were illuminated by a co-planar pair of 530 nm sheet lasers. The resulting images were then processed in the MATLAB PIVlab app (Thielicke & Sonntag 2021).

An additional step to help visualise the flow draws on consecutive frame differencing based motion detection to develop streak line images. In this process, a set of n consecutive frames is loaded into an in-house developed MATLAB code and the absolute value of the difference between pixel values in pairs of consecutive frames is calculated. Doing this creates a series of $n - 1$ frames where the only bright pixel values are those that correspond to the location of objects that have moved during the interval between frames. When used in the experiments discussed here, the motion detected was primarily that of the seeding particles used for PIV, although some of the prism's motion was also captured. However, since the prism was moving within the frame at a lesser rate than the seeding particles, the prism motion was not as visually significant. The sum of this series of frames was then subtracted from a pure white frame to create a new image that showed streak lines of the particles. The same masking image used in PIV processing was applied to this image to show the location of the prism. The frame difference streak line images were stacked on top of the vorticity field calculated in the PIV processing to better highlight the overall influence of the prism on the wake in the flow visualisation images, especially to enable observation of the details in the wake.

The mass ratio of the prism, defined as the moving mass of the solid, m, divided by the displaced mass of the fluid, $m^* = m/(\sqrt{3}\rho S^2 L/4)$, where ρ is the fluid density, was measured to be $m^* = 1.2$. The moment of inertia of the entire rotating assembly, including the prism, top and bottom plates, top and bottom axles, and spring pulley, was 3×10^{-3} kg m^2, and the mass of the assembly was 407 g. The natural frequency and damping ratio of the system in air were measured using a decay test to be $f_n = 0.81$ Hz and $\zeta = 0.021$, respectively. The natural frequency of the system in water depends on the specific case and orientation in question. Case 1 in the concave orientation and Case 2 in the convex orientation have the same natural frequency of $f_{nw} = 0.73$ Hz since these two cases share the configuration where a flat side of the prism is closer to the axis of rotation. Similarly, Case 1 in the convex orientation and Case 2 in the concave orientation share a natural frequency of $f_{nw} = 0.71$ Hz since they both have an edge of the prism nearest to the axis of rotation. Case 3 has a natural frequency of $f_{nw} = 0.67$ Hz for both orientations. The experiments were conducted over a Reynolds number range of $640 < Re < 7940$, defined with the side of the prism as the characteristic length.

To examine the mechanisms that cause the variations in the system response observed for the different cases, the flow-induced torque acting on the prism was calculated through inverse dynamics, expanding on the method presented by Khalak & Williamson (1999), and independently validated in previous work by one of the authors of this paper
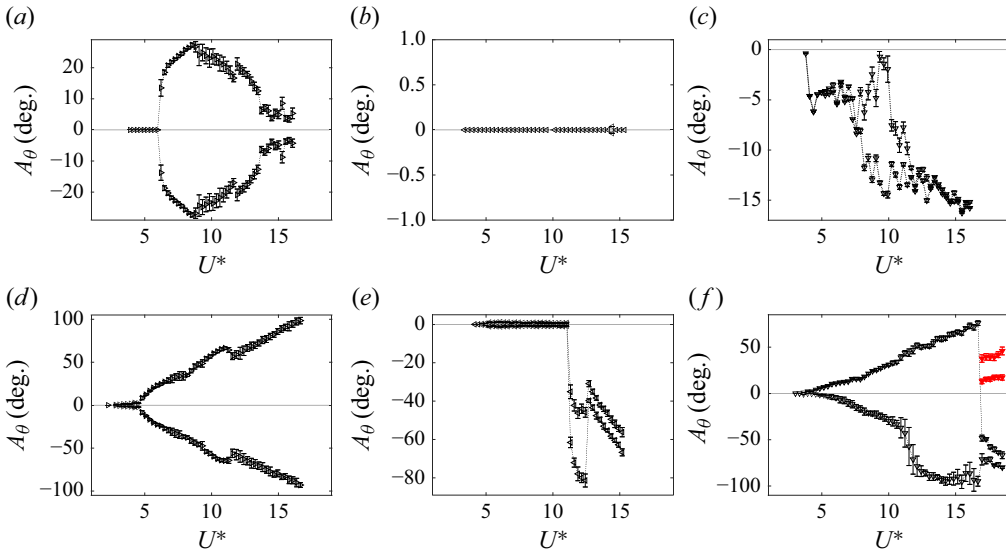
Figure 2. Amplitude of response versus reduced velocity for the triangular prism in a (*a–c*) concave orientation and (*d–f*) a convex orientation and for cases where the prism is initially placed such that (*a,d*) one side sees the flow first (Case 1), (*b,e*) one edge sees the flow first (Case 2) and (*c,f*) one side of the prism is placed parallel to the incoming flow (Case 3). In panel (*f*), in addition to the natural response of the system shown in black, there are red markers indicating an alternate branch of oscillations, with a mean position of $\theta \approx 27°$ that is stable if the prism is manually placed in that region.

(Seyed-Aghazadeh, Carlson & Modarres-Sadeghi 2015). In this method, the velocity and acceleration of the system are calculated from the displacement time series, and, with the measured natural frequency and damping of the system, the equation of motion for a forced 1-DOF angular oscillator is used to calculate the torque acting on the system, as

$$\tau = I_0\ddot{\theta} + c\dot{\theta} + k\theta. \tag{2.1}$$

The phasing, ϕ, of the first harmonic of the forces relative to the displacement, velocity and acceleration can then be calculated, as shown by Bourguet & Jacono (2014). These phases are discussed later in the text for all three cases in both the concave and convex orientations.

3. An overview of the prism response

We consider three different cases based on the initial angle that the triangular prism makes with the direction of the incoming flow. Case 1, when one of the sides of the prism sees the flow first; Case 2, when one of the edges of the prism sees the flow first; and Case 3 when one of the sides of the prism is parallel to the incoming flow, as illustrated in figure 1. For each case, we consider both a concave path, where the axis of rotation is upstream of the prism, and a convex path, where the axis of rotation is downstream of the prism. Figure 2 shows the amplitude of the observed response for all these six cases versus reduced velocity, where the triangle's side is used as the length scale, and figure 3 shows their corresponding frequencies. These amplitude plots show the mean amplitude of angular displacement across each cycle of oscillations, and the error bars represent ±1 standard deviation. Note that the *y*-axis ranges in the amplitude plots change for different cases to show the details of how the amplitude varies versus the reduced velocity
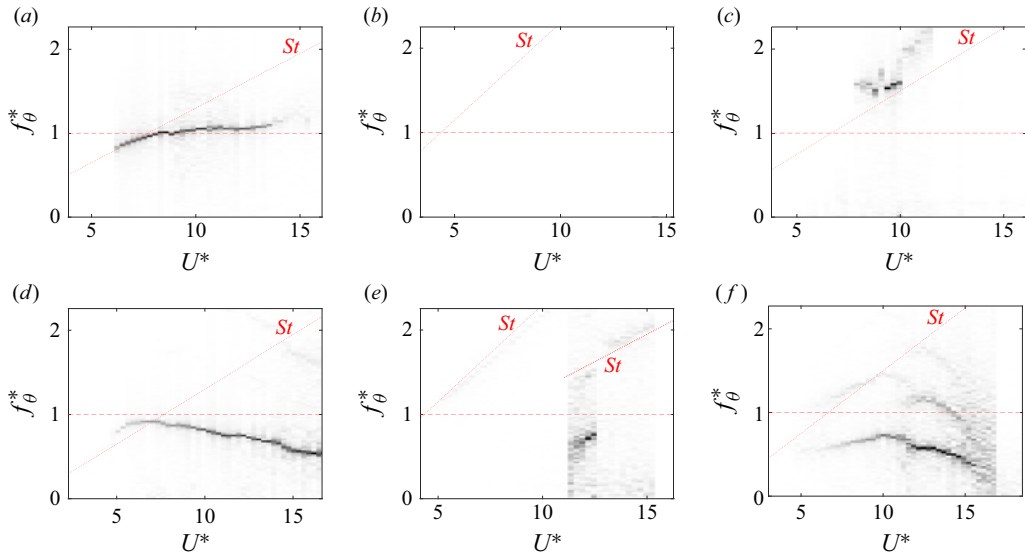
Figure 3. Frequency of response versus reduced velocity for (*a–c*) the triangular prism in a concave orientation and (*d–f*) a convex orientation and for (*a,d*) Case 1, (*b,e*) Case 2 and (*c,f*) Case 3. The dashed red lines show the natural frequency of the system, and the dotted red lines show the predicted Strouhal shedding frequencies, based on Strouhal numbers of (*a,d*) 0.13, (*b*) 0.23, (*c,f*) 0.15. For panel (*e*), the prism takes on a large mean displacement at $U^* \approx 11.3$, changing the mean angle of attack of the prism. To account for this, two Strouhal lines are drawn, using the relevant Strouhal numbers of 0.23 and 0.13 for the regions below and above this critical reduced velocity, respectively.

in each case. The inclined dashed lines in the frequency plots of figure 3 correspond to the Strouhal frequency, f_{St}, using the Strouhal number, St, for a fixed triangular prism with the relevant orientation with respect to the flow for each case found by Seyed-Aghazadeh *et al.* (2017). These values are $St = 0.13$ for Case 1, $St = 0.23$ for Case 2 and $St = 0.15$ for Case 3. As we will discuss in § 5.2.2, in the convex orientation of Case 2, there is a critical reduced velocity above which the prism deflects to one side and oscillates about a non-zero mean value of θ. A second dashed line is plotted in figure 3(*e*) for these reduced velocities to show the predicted shedding frequency based on $St = 0.13$, the Strouhal number corresponding to the mean angle of attack for the prism in this reduced velocity range.

A quick glance at these results clarifies that the change in initial condition has a significant influence on the observed response. In one case, no oscillations are observed at all, while in some other cases, amplitudes of over 90° are observed. In some cases, the response stays symmetric, while in other cases, a static deflection is observed with oscillations about this static mean, or with no oscillations about the static deflection. In what follows, we will focus on the details of these responses and discuss their differences and the vortex patterns that are observed in their wakes.

4. Case 1 (when one side sees the flow first)

In this case, the neutral angle of attack for the prism is set such that one side is on the upstream side and perpendicular to the incoming flow. This configuration is presented first as it demonstrates a purely VIV response in the concave orientation and a VIV transitioning to galloping response in the convex orientation, both of which are relatively familiar behaviours.
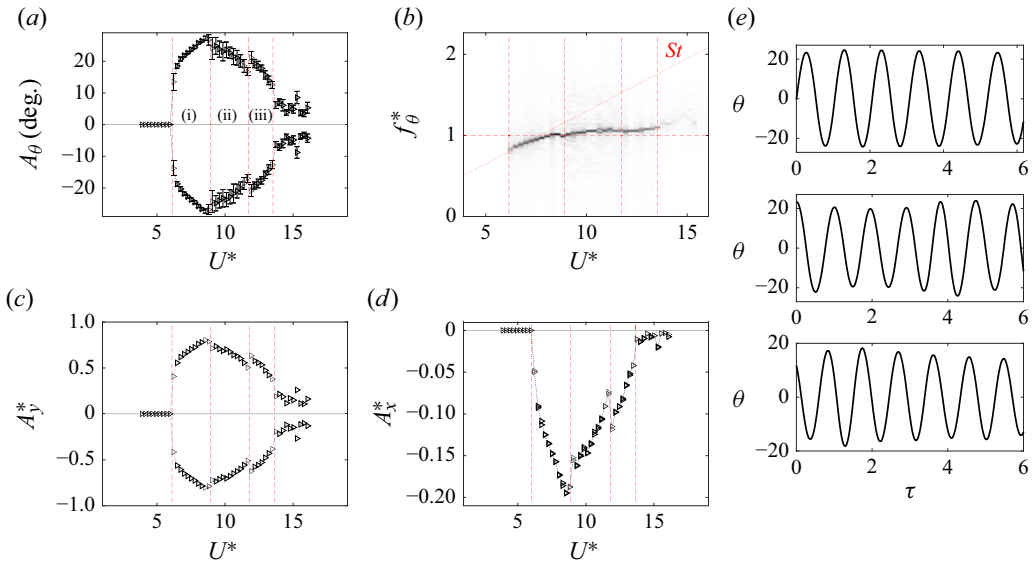
Figure 4. Case 1 in the concave orientation: (*a*) amplitude of angular oscillations; (*b*) the frequency content of oscillations; (*c*) the cross-flow and (*d*) the inline amplitudes versus the reduced velocity. The vertical lines in panels (*a–d*) show the three different regions of the lock-in range. Panel (*e*) shows representative time series from each region of the response, at $U^* = 7.5$, $U^* = 10.6$ and $U^* = 13.0$ from top to bottom, respectively. The horizontal axes are non-dimensional time, $\tau = t f_{nw}$.

4.1. *In the concave orientation*

The amplitude and frequency plots of this case are shown in figure 4. In these plots, the amplitude and frequency of angular oscillations are shown in the plots of the upper row. In the lower row, the amplitudes of oscillations in the IL, x, and CF, y, directions are shown, which are the displacements of the centre of gravity of the prism. These values correspond to the components of the prism's oscillations in these directions, and can be used to compare these oscillations with those typically reported in VIV studies of 1- or 2-DOF systems with purely translational motions. These plots show that in the concave orientation, the response resembles that of a typical VIV response in which lock-in is observed over a range of reduced velocities, here, $U^* \approx 7$ to $U^* \approx 15$, during which a synchronisation between shedding frequency and oscillation frequency has occurred. This lock-in range has three distinct regions, differentiable by the frequency and consistency of amplitude of oscillations. These regions are highlighted by the vertical dashed lines in the figure and are discussed with some details in what follows.

4.1.1. *Region 1*

In the first portion of the lock-in range, at the onset of oscillations, the prism oscillates at a frequency matching the shedding frequency predicted by the Strouhal number measured by Seyed-Aghazadeh *et al.* (2017), which is approximately $0.9 f_{nw}$. As the reduced velocity is increased, the frequency of oscillations increases until it reaches the structure's natural frequency. At this point ($U^* \approx 9$), the amplitude of oscillations reaches a maximum value of approximately $27°$, which corresponds to maximum cross-flow and inline displacements of $A_y^* = \pm 0.8$ and $A_x^* = -0.2$, respectively.

Just after the onset of oscillations, at $U^* = 7.0$, a 2S shedding pattern is observed in the wake where one vortex is shed at each maximum displacement of the prism during each
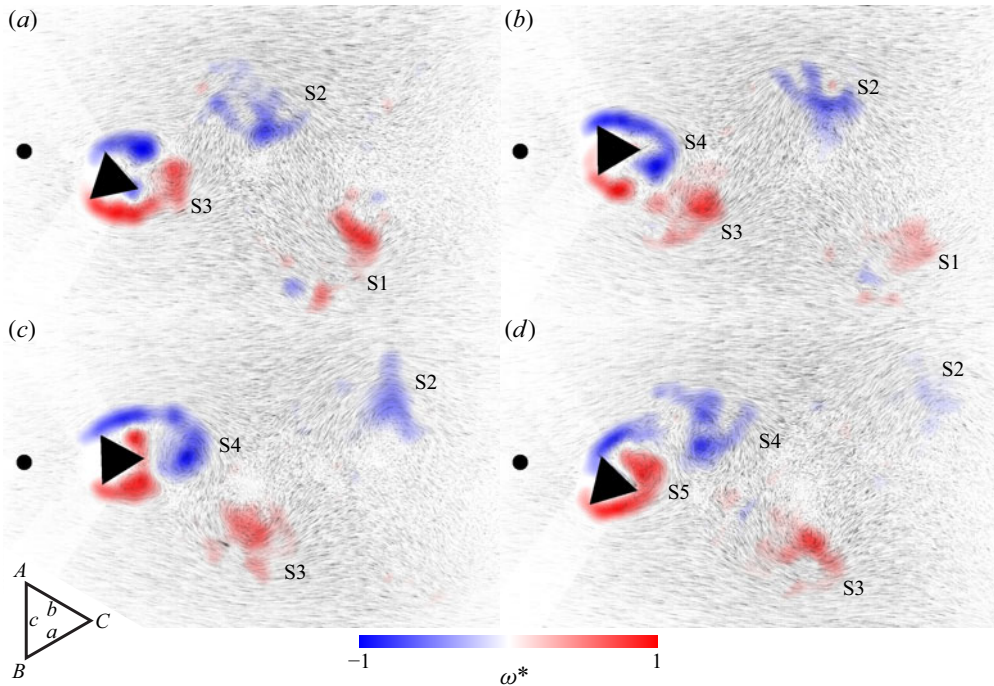
Figure 5. Snapshots of the wake for Case 1 in the concave orientation at $U^* = 7.0$, with positive vorticity in red and negative vorticity in blue. The maximum vorticity magnitude in these snapshots is $\omega = 31.7\,\mathrm{s}^{-1}$. In addition to the vorticity, these snapshots show the streaklines generated from the experimental recordings using the method outlined in § 2. Video of this example is shown in supplementary movie 1.

cycle. During the cycle of oscillations shown in figure 5, as the prism begins to move in the $+\theta$ direction, vortices S1 and S2 have been shed and are travelling downstream while a new vortex, S3, is shed from edge C. The shear layer separates at edge B then reattaches to the trailing side (side a). A negative vortex is formed around edge C in figure 5(b). This trailing edge vortex, which rotates in a direction opposite the prism rotation, interacts with the shear layer that is passing side a and diverts it back towards the prism, and causes the reattachment as the prism continues to move in the counterclockwise (CCW) direction (figure 5b). In figure 5(c), the prism moves in the clockwise (CW) direction, vortex S4 is shed, as a gap is observed between the vortex core and the shear layer coming off of edge A. Meanwhile, a bound vortex is developed on sides a and b and is shed from the downstream edge (C) of the prism (S5) as observed in panel (d). Therefore, a 2S pattern is observed in the wake, where one vortex is shed at each maximum displacement of the prism. While this wake pattern is the same as what has been observed in the past in the wake of a cylinder experiencing cross-flow VIV, it differs in that a significant portion of the fluid that makes up the vortices in the present case has in fact travelled around the far side of the prism before forming the vortex.

At higher reduced velocities, towards the end of the first region of the lock-in range, the oscillations are at their largest magnitude, the reattachment of the shear layers that separate from the upstream edges (A and B) is delayed and small additional vortices are shed from these edges as well. This then results in the formation of a 2C shedding pattern in the wake of the prism, where two vortices, rotating in the same direction, are shed during each half-cycle of oscillations. The vortices that are shed from edges A and B cause the wake to widen in the cross-flow direction as they travel downstream, whereas the vortices shed
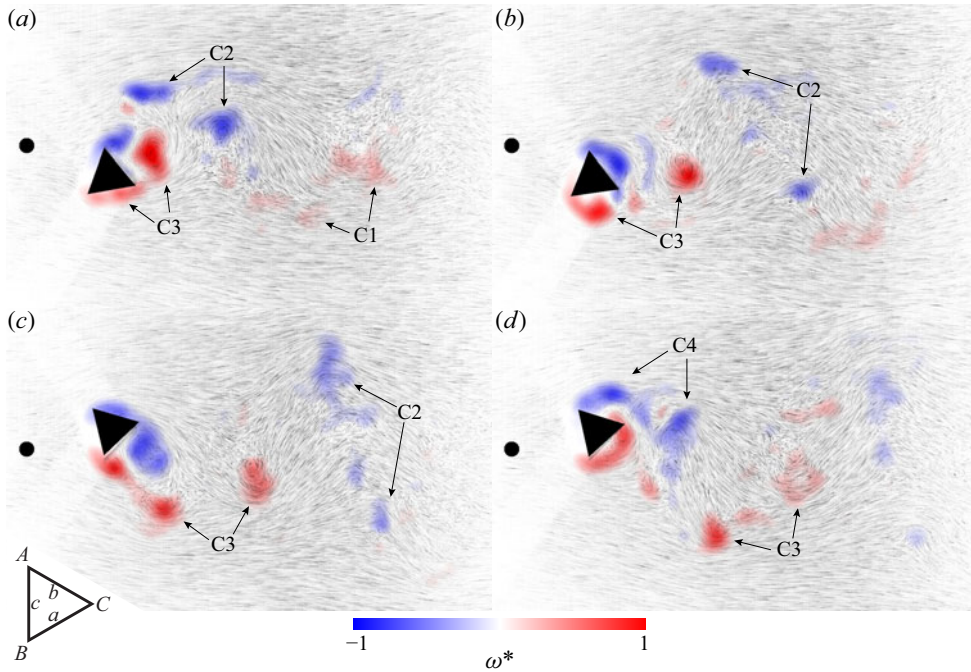
1023 A5-10

Figure 6. Snapshots of the wake for Case 1 in the concave orientation at $U^* = 9.1$ over a half-cycle of oscillations. The maximum vorticity magnitude in these snapshots is $\omega = 57.0\,\text{s}^{-1}$. This reduced velocity corresponds to the largest oscillation amplitude observed for this case.

from the downstream edge (C) travel downstream parallel to the incoming flow. Figure 6(a) shows the prism approaching its maximum clockwise displacement, with two pairs of co-rotating vortices in the wake, C1 and C2. A third pair, C3, is still attached to the prism. In panel (b), the prism has begun its sweep back across the flow, causing the vortices of C3 to separate, while the CW vortex attached to the prism has begun to wrap around the downstream side. In panel (c), the prism is approaching its maximum CCW displacement and the blue vortices are being formed and later shed as another pair of C vortices in panel (d).

4.1.2. *Region 2*

For reduced velocities within the second region of the lock-in range, $9.1 < U^* < 11.9$, the oscillation amplitude decreases with increasing reduced velocity, while the oscillation frequency stays relatively constant, as shown in figure 4(a,b), at a value slightly larger than the structure's natural frequency. This region of the lock-in range is characterised by larger variations in oscillation magnitude cycle to cycle, corresponding to greater inconsistency in the shear layer behaviour than that in the first region of the lock-in range. In some cycles, the shear layer reattachment occurs quickly, in other cycles, it may not occur until the prism has already traversed most of the way across the arc as it cuts through the flow. As the shear layer grows in length and the gradient across it increases, small vortices appear in the shear layer. These small vortices get entrained in the larger vortices that are formed in the wake, resulting in a 2S shedding pattern. A sample of this shedding formation is given in figure 7. In panel (a), vortices S1 and S2 have been shed and are travelling downstream, while vortex S3 is forming and still attached to the prism, which is at the maximum extent of its clockwise displacement. As the prism begins moving counterclockwise, vortex S3 is shed and a clockwise vortex begins developing off of the downstream side of the prism, shown
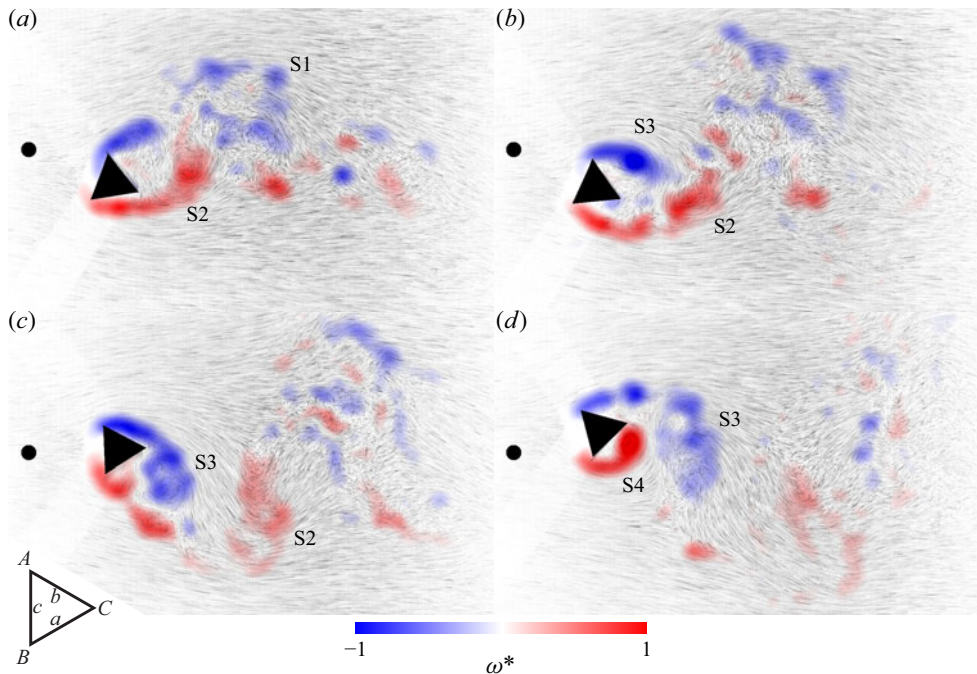
Figure 7. Snapshots of the wake for a half-cycle of oscillations for Case 1 in the concave orientation at $U^* = 11.0$. The maximum vorticity magnitude in these snapshots is $\omega = 65.5\,\text{s}^{-1}$.

in panel (*b*). Panel (*c*) corresponds to the wake after the prism has reached its maximum counterclockwise displacement and has begun moving clockwise again. This motion has resulted in shedding of vortex S4, which moves downstream in panel (*d*). Unlike for the 2S pattern observed at $U^* = 7.0$, the numerous small vortices that have appeared in the shear layers result in larger vortices (labelled S1–4) that are less concentrated and therefore dissipate quickly after formation.

4.1.3. *Region 3*

At $U^* = 11.9$, there is a sudden increase in the amplitude of oscillations as the prism enters the third region of the lock-in range (figure 4). This amplitude jump corresponds to the beginning of a region of oscillations wherein the frequency increases linearly with reduced velocity, while the amplitude decays from $A_\theta = 21°$ to $A_\theta = 12°$ at $U^* = 13.5$, after which the lock-in range ends.

In this region, the reduced velocity is high enough that the shear layer never reattaches and, therefore, the shedding occurs from the two upstream edges (*A* and *B*) in a 2S pattern with a relatively long formation length. The onset of this flow behaviour corresponds to the initial jump in the oscillation amplitude. Ultimately, the reduced velocity is increased to the point where vortex shedding de-synchronises with the prism oscillation and the amplitude of oscillations drops dramatically for $U^* > 13.5$.

4.2. *In the convex orientation*

In this orientation, the prism is mounted upstream of the pivot point, such that any angular displacement causes a downstream displacement as well. The response in the convex orientation is very different from the response in the concave orientation: at higher reduced velocities, galloping is observed. Once again, there are three distinct regions in the
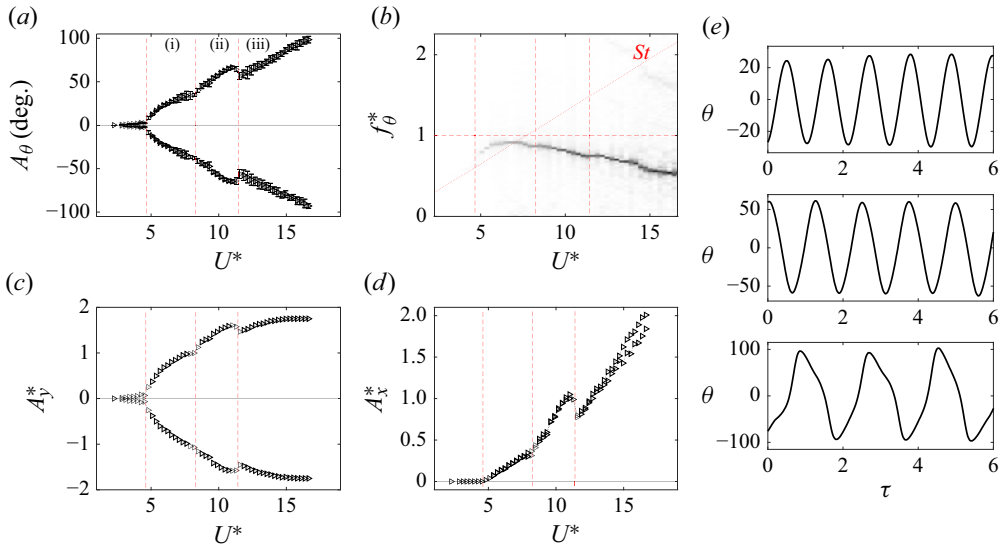
Figure 8. Case 1 in the convex orientation: (*a*) amplitude of angular oscillations; (*b*) frequency content of oscillations; (*c*) cross-flow; and (*d*) inline amplitudes versus the reduced velocity. The vertical lines in panels (*a*–*d*) show the three different regions of the prism response, VIV, transitional and galloping. These regions correspond to different vortex shedding patterns. Panel (*e*) shows representative time series from each region of the response, at $U^* = 6.5$, $U^* = 10.1$ and $U^* = 16.6$ from top to bottom, respectively.

amplitude response, as highlighted in figure 8. We will discuss the details of the system's response in each of these regions in what follows.

4.2.1. *Region 1*

The first region is from the onset of oscillations at $U^* \approx 4.7$ to $U^* \approx 8$, where a response similar to what is observed in the VIV response of bluff bodies is observed. The frequency of oscillations begins at approximately $0.8 f^*$, but quickly increases to approximately $0.9 f^*$, where it stays throughout this region of the lock-in range.

In this region, flow stays attached to the leading side of the prism on the downstream side. In figure 9(*a*), where the prism has just begun moving in the clockwise direction, two vortex pairs, P1 and P2, are already in the wake, and another pair, P3, is being shed in the form of two vortices, one from the upper side and the other from the front side of the prism. In figure 9(*b*), the flow is still attached to side *b*, and the flow that separates from the trailing edge *B* is directed back towards the trailing side *a* by the negative vortex of pair P3, causing the flow to reattach to side *a*. As the prism approaches its maximum displacement and begins to slow down (figure 9*c*), the flow separates from side *b* and a vortex is shed from edge *A*. At the same time, the separation bubble on side *a* collapses and the bound vortex that is forming around edge *B* flows down on side *a* to edge *C*, where it sheds as a CCW vortex, forming the new vortex pair P4 with the vortex that was shed from edge *A*. The region of flow between this vortex pair is directed back towards side *b*, causing reattachment of the shear layer that separated from edge *A* as the prism begins moving in the CCW direction, as seen in figure 9(*d*), where P4 moves away from the prism and the positive vortex for the next pair to be shed has begun forming around edge *B*. While this alternating arrangement of attached shear layer and separation bubble on sides *a* and *b* is similar to that seen in the first region of the lock-in range of the concave orientation (see figure 5), the fact that the angle of attack of the prism is changing in the
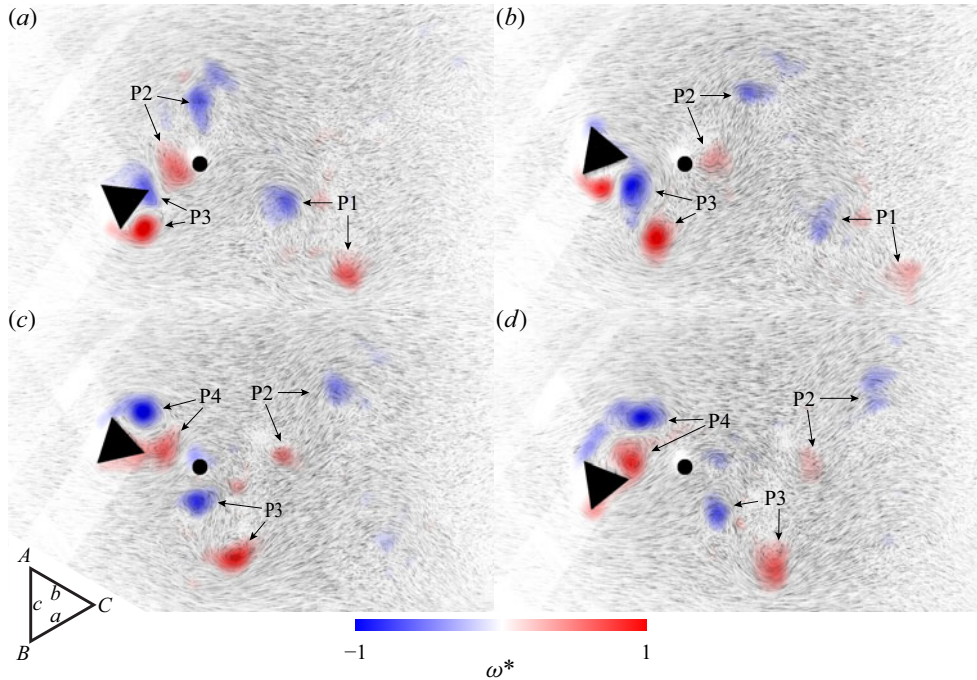
Figure 9. Snapshots of the wake for Case 1 in a convex orientation at $U^* = 6.2$. The maximum vorticity magnitude in these snapshots is $\omega = 56.1\,\text{s}^{-1}$. A 2P vortex pattern is observed in the wake, where a pair of counter-rotating vortices is shed from the prism during each half-cycle.

same direction as the displacement in this orientation (i.e. increasing θ increases α) and in the opposite direction in the concave orientation (where increasing θ decreases α) is what causes the change in separation and reattachment timing, and therefore the change in shedding patterns.

4.2.2. *Region 2*

In the transition region, from $U^* \approx 8$ to $U^* \approx 11$, there is an increase in the rate at which the oscillation amplitude grows. Beyond $U^* \approx 11.5$, and up to the maximum U^* tested here, the amplitude increases linearly, which is the typical behaviour in a galloping response. The maximum amplitude reaches nearly $100°$, $A_y^* = 1.75$ and $A_x^* = 2$. We refer to the region in between the VIV response and the galloping response as the transition region. This transition from VIV to galloping is observed in the frequency response of the system as well. Initially, when VIV starts, the observed normalised frequency is close to 1, and the synchronisation starts close to the intersection between the Strouhal frequency line and $f^* = 1$, as observed in the typical VIV responses. The frequency immediately begins a monotonic decrease from this point as the reduced velocity is increased, suggesting a steady transition towards a galloping response.

In this region, the timing of the reattachment of the shear layer on the trailing side is delayed due to both the increase in flow velocity and the larger magnitude of oscillations, and the shedding pattern becomes 2P + 2S. The amplitude of oscillations here approaches $\theta \approx 60°$, which causes the orientation of the prism at its maximum displacement to be similar to Case 2 relative to the incoming flow. As will be discussed in § 5, this orientation causes the development of strong shear layers that keep the vortex formed around edge C attached to the prism and delays the timing of the shedding. The outermost edges of the
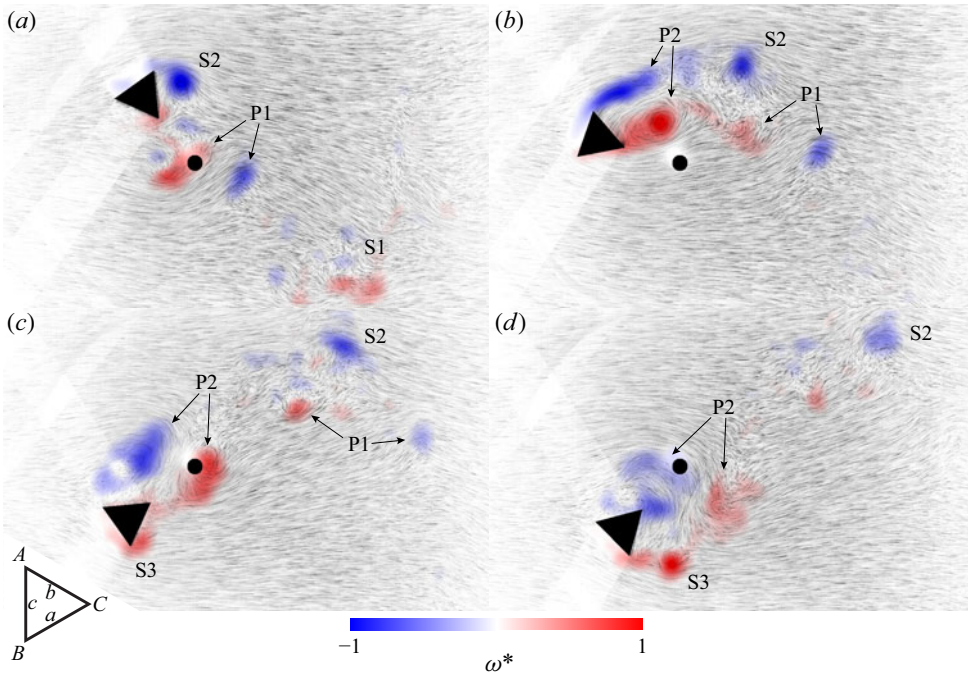
Figure 10. Wake snapshots for Case 1 in the convex orientation at $U^* = 9.8$. The maximum vorticity magnitude in these snapshots is $\omega = 65.2\,\mathrm{s}^{-1}$. Here, the prism exhibits a 2P + 2S shedding pattern in its wake. Video of this example is shown in supplementary movie 2.

prism (A at the maximum negative θ position and B at the maximum positive θ position) still shed a single vortex each as the prism slows and reverses direction. Figure 10(a) shows a single vortex (S1) and a pair of vortices (P1) that have been already shed as the prism traversed the flow, and a new single vortex (S2) that is being shed from edge A as the prism slows and ultimately stops. As the prism travels in the CCW direction in figure 10(b), the shear layers that have separated from edges A and C form a second pair of vortices (P2) as side b becomes parallel with the incoming flow in figure 10(c), where another single vortex (S3) is shed, before the prism begins returning towards its neutral position in panel (d). There are two significant differences between the arrangement of these vortex pairs in this region in comparison with the vortex pairs observed in region 1. First, as the shedding occurs closer to $\theta = 0°$ than in the first region of the response, the vortices stay closer to $y^* = 0$ than in the first region. Second, the vertical distance between the vortex cores themselves is reduced relative to that observed in the first region of response: the angle between vortex cores in each pair is $\sim 45°$ in figure 9 in comparison with $\sim 10°$ in figure 10.

4.2.3. *Region 3*

The galloping response becomes the main response of the system starting at $U^* \approx 11.5$ after which, the amplitude of oscillations increases linearly with reduced velocity. In this region of the response, the shedding of vortices and the oscillation frequency are not synchronised, as expected in a galloping response. The snapshots of the wake at $U^* = 14.0$ are given in figure 11. When the prism goes downward from its uppermost position, it sheds three blue vortices and two red vortices, and in its following half-cycle, it sheds three red vortices and two blue vortices. This is typical of a galloping case in which the
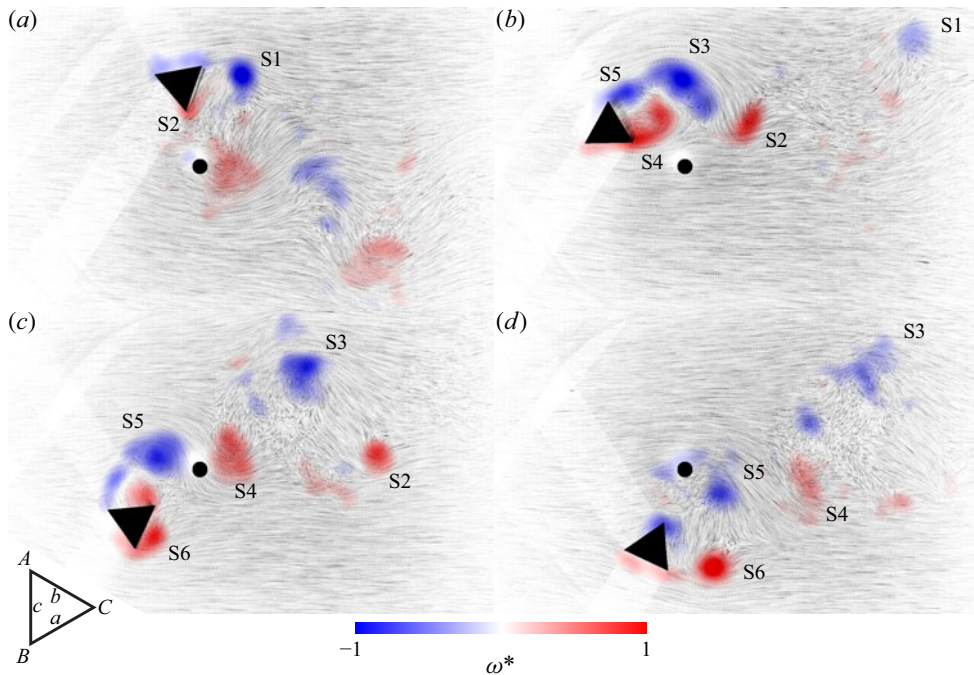
Figure 11. Snapshots of the wake for Case 1 in the convex orientation at $U^* = 14.0$. The maximum vorticity magnitude in these snapshots is $\omega = 85.4\,\mathrm{s}^{-1}$. At this reduced velocity, the prism is galloping and the synchronisation between vortex shedding and structural oscillations has ceased.

shedding of vortices is a result of the presence of the bluff body in the flow and not the cause of its oscillations – the oscillations are observed due to a negative flow induced damping that acts on the structure. In figure 11(*a*), the prism is beginning to travel in the CCW direction and has shed a negative vortex (S1), while a small positive vortex (S2) is forming on the downstream side, which is now fully exposed to the incoming flow due to the large amplitude of oscillations. This vortex (S2) is quickly shed, along with two others (S3 and S4) by the time the prism approaches $\theta = 0°$ in panel (*b*). As the prism crosses its neutral position in panel (*c*), a negative vortex, S5, sheds and another vortex (S6) forms attached to side *a*. This vortex is shed when the prism reaches its maximum displacement in panel (*d*) and is analogous to S1. In total, five vortices are shed in each half-cycle, for a total of ten single vortices shed per oscillation cycle.

5. Case 2: when the sharp edge sees the flow first

In this case, the prism is oriented inversely to that in Case 1, such that one edge of the prism points directly upstream and the downstream side is perpendicular to the flow. This initial condition is equivalent to the $\alpha = 0°$ case described by Seyed-Aghazadeh *et al.* (2017).

5.1. *In the concave orientation*

In this case, when the prism is placed in a concave orientation, no oscillations are observed. Any given initial disturbance to the structure damps down to zero oscillations and the structure stays still. This resembles the response of a triangular prism allowed to oscillate on a straight line. In that case, when the angle of attack is set to zero, the prism does not
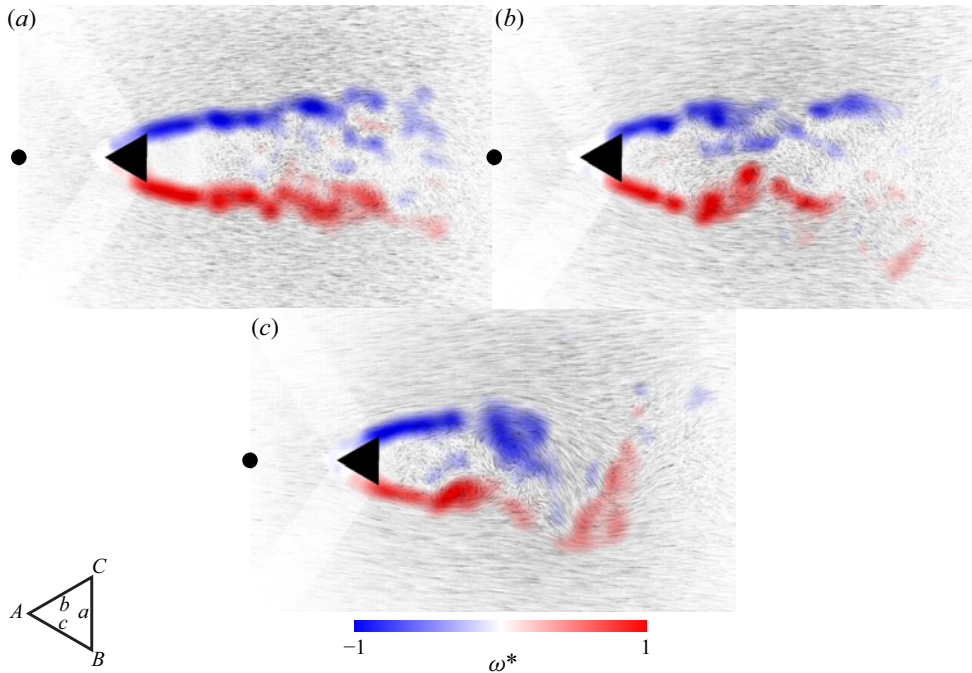
Figure 12. Snapshots of the wake for Case 2 in the concave orientation at (*a*) $U^* = 6.1$, (*b*) $U^* = 8.9$ and (*c*) $U^* = 12.9$. The maximum vorticity magnitudes in these snapshots are $\omega = 18.4\,\mathrm{s}^{-1}$, $\omega = 30.9\,\mathrm{s}^{-1}$ and $\omega = 38.4\,\mathrm{s}^{-1}$, respectively. Video of the $U^* = 8.9$ example is shown in supplementary movie 3.

oscillate (Seyed-Aghazadeh *et al.* 2017). Sample snapshots of the wake of the prism in this case are given in figure 12. In this case, the flow separates at the two downstream edges of the prism. At lower reduced velocities, the prism creates strong shear layers that propagate downstream, with small vortices forming within the shear layers. As the reduced velocity is increased, the shear layers begin to roll up into larger vortical structures, and at still higher reduced velocities, these structures coalesce into a 2S shedding pattern. However, the formation length for these vortices is quite long and therefore these shed vortices do not produce significant enough fluctuating forces on the prism to cause oscillations.

5.2. *In a convex orientation*

In the convex orientation, however, the behaviour is quite different. The response for this arrangement has three distinct regions as highlighted in figure 13. Above a critical reduced velocity, the flow forces on the prism cause a mean displacement, which significantly influences the shedding patterns and induces oscillations comparable in magnitude to those observed in Case 1 placed in the concave orientation. Here, we discuss the response of the prism in these three regions.

5.2.1. *Region 1*

Below $U^* = 10.5$, there are only very small oscillations, where $A_\theta \approx 1°$. This is enough to change the wake of the prism compared with the concave orientation, where very long shear layers are formed. Instead, in this convex orientation, the shear layers form a 2S pattern in the near wake. Sample snapshots of the wake in this region of the response are shown in figure 14. This shedding is synchronised with the small oscillations of the prism, but they do not lock-in at the structural natural frequency and instead follow the predicted
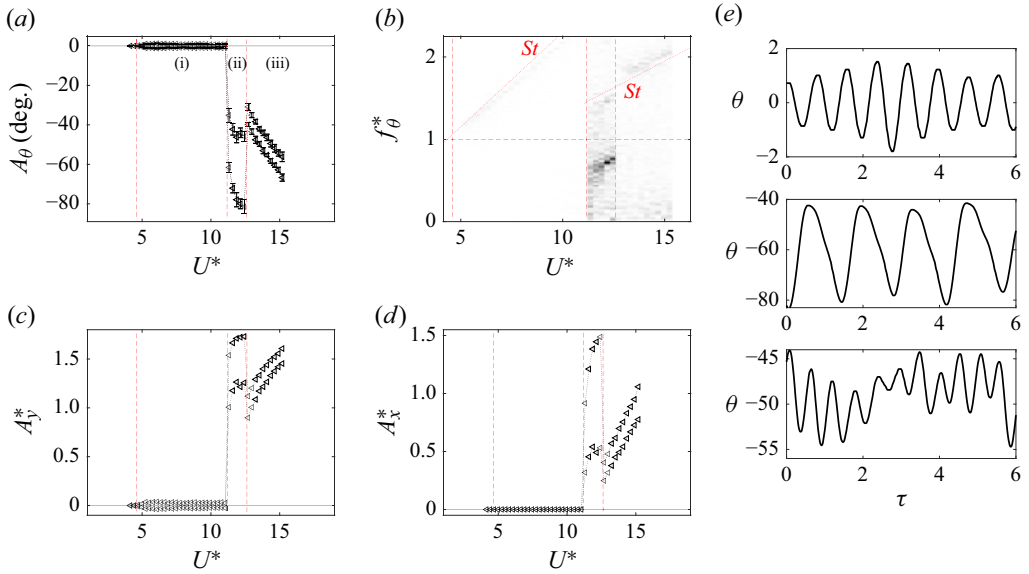
Figure 13. Case 2 in the convex orientation: (*a*) amplitude of angular oscillations; (*b*) frequency content of oscillations; (*c*) cross-flow; and (*d*) inline amplitudes versus the reduced velocity. The vertical lines in panels (*a–d*) show the three different regions of the lock-in range. Panel (*e*) shows representative time series from each region of the response, at $U^* = 5.8$, $U^* = 12.1$ and $U^* = 13.8$ from top to bottom, respectively.

Strouhal shedding frequency as can be seen in figure 13(*b*). Therefore, while these small oscillations occur at the reduced velocity range in which one would expect a VIV response, these small-amplitude oscillations are not VIV.

5.2.2. *Region 2*

As the reduced velocity is increased to $U^* = 11.3$, $\theta = 0°$ becomes an unstable position, and any slight perturbation from the flow deflects the prism far to one side, to a mean value of $\theta \approx -50°$, and the prism begins to oscillate about this new mean displacement. The result is that instead of one edge of the prism seeing the incoming flow first, one of the sides does, similar to Case 1, and the shedding frequency decreases, corresponding to a change in Strouhal number from $St = 0.23$ to $St = 0.13$ as determined by Seyed-Aghazadeh *et al.* (2017). The dashed line in the frequency plot of figure 13, which corresponds to the predicted shedding frequency using this new Strouhal number, makes it apparent that the oscillations are synchronised with $f_{St}/2$.

The time histories of angular displacement in this region of the response exhibit an asymmetric waveform that is closer to a saw-toothed waveform than a sinusoidal one. Figure 13(*e*) shows the time history for the prism at the reduced velocity corresponding to the largest oscillation magnitude, where the mean displacement is approximately $-65°$ and oscillations follow a saw-toothed waveform. The motion of the prism in the positive θ direction is noticeably faster than in the negative direction, in spite of the fact that this motion is in the direction opposite to the direction of incoming flow.

Snapshots of the wake for one full cycle of oscillations in this case are shown in figure 15. At the start of the cycle (panel *a*) the prism is at its extreme upward path and the shear layer that originates from edge *A* and stays attached to side *b* is just separated to form a single vortex S1 in the wake. As this vortex is shed, the prism begins to move rapidly back towards $\theta = 0°$. Meanwhile, the shear layer that separates at edge *B* wraps
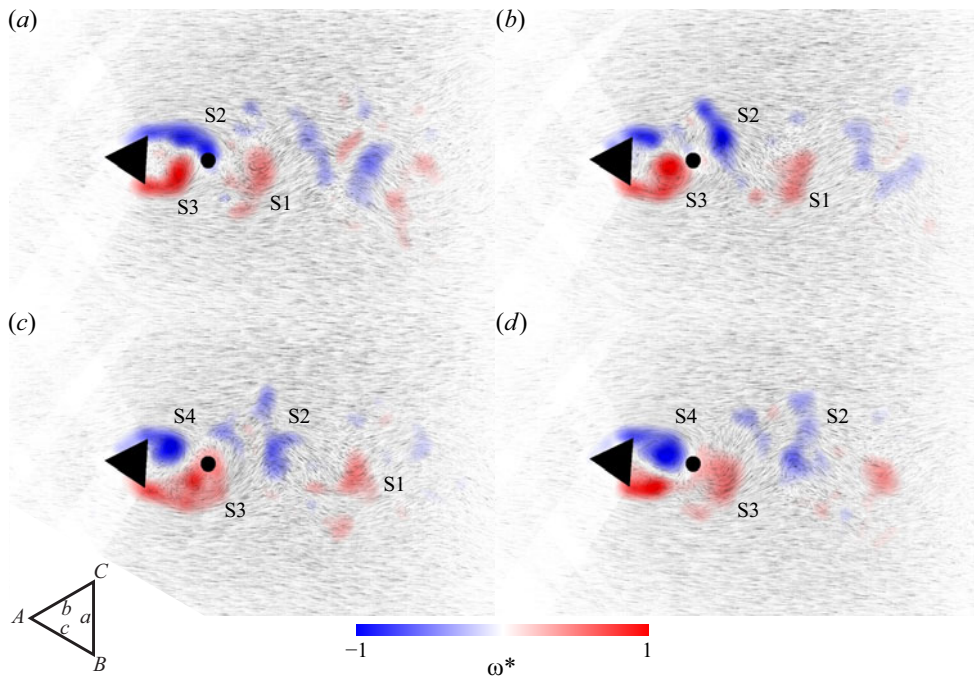
Figure 14. Snapshots of the wake for Case 2 in the convex orientation at $U^* = 6.6$. The maximum vorticity magnitude in these snapshots is $\omega = 33.6\,\mathrm{s}^{-1}$.

around a separation bubble on side a and passes by edge C, filling the area left behind by the shedding of S1, before being shed to form vortex S2. In figure 15(b), the prism has reached its minimum displacement, and at this point, the flow stays attached to side b and vortices begin to shed from edges B and C. The angle of side c directs the flow downwards and the flow reattaches to side b, the combination of which causes the prism to be slowly deflected back clockwise (figure 15c). During this motion, a series of vortices (S2–S6) are shed from edges B and C, until the prism reaches its extreme upward path (panel d) when it snaps back again, and restarts the cycle. This highly asymmetric behaviour can be viewed as a mix of VIV and galloping, where the first half-cycle acts similar to a typical VIV response with a single vortex shed in that half-cycle (S1 in panel a) and the second half-cycle acts as a galloping response, where the shedding frequency is much higher than the frequency of oscillations.

5.2.3. *Region 3*

At higher reduced velocities, oscillation amplitudes and the mean displacement drop and the prism exhibits erratic oscillations about a new mean (figure 13e). These oscillations no longer have the saw-tooth waveform that characterised the time series of the response in the previous region and occur at a frequency near that predicted for shedding frequency using the Strouhal number for the mean displacement of the prism, with a broad range of low frequencies. In this range of reduced velocities, the shear layers separating from edges A and B never reattach, reducing the fluctuating lift forces on the prism and explain the reduction of mean displacement and mean amplitude. When the shear layer attaches to side b, it creates a larger lift force in the $+y$ direction, which pulls the prism in the same direction as the drag pushes it, in region 2. In this region, the mean displacement is due to the drag force, which explains the steady increase in the mean displacement
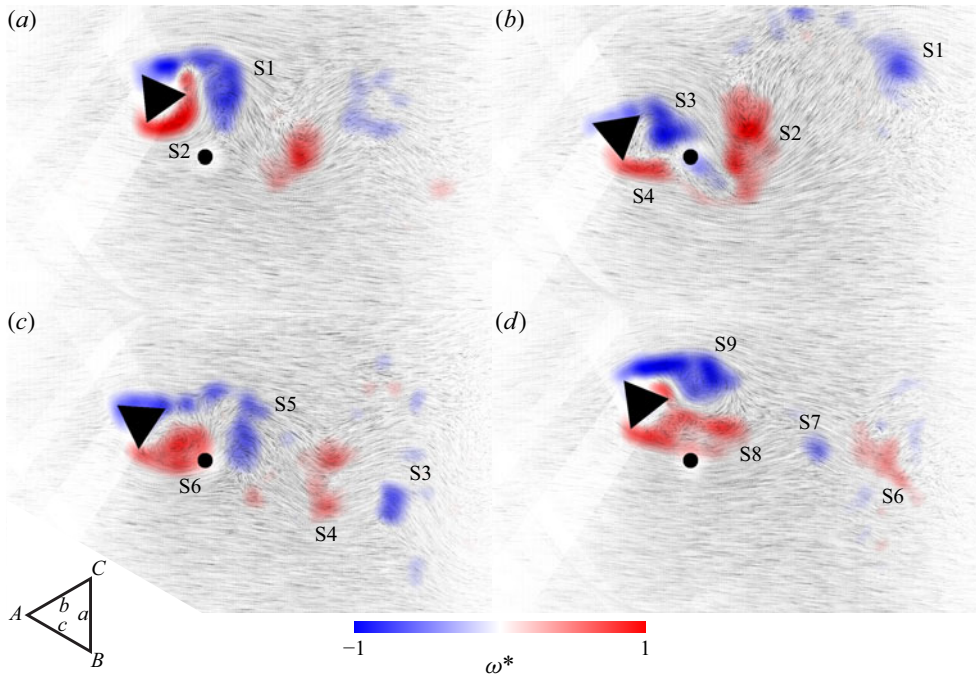
Figure 15. Snapshots of the wake for Case 2 in the convex orientation at $U^* = 11.9$. The maximum vorticity magnitude in these snapshots is $\omega = 52.6\,\text{s}^{-1}$. Video of this example is shown in supplementary movie 4.
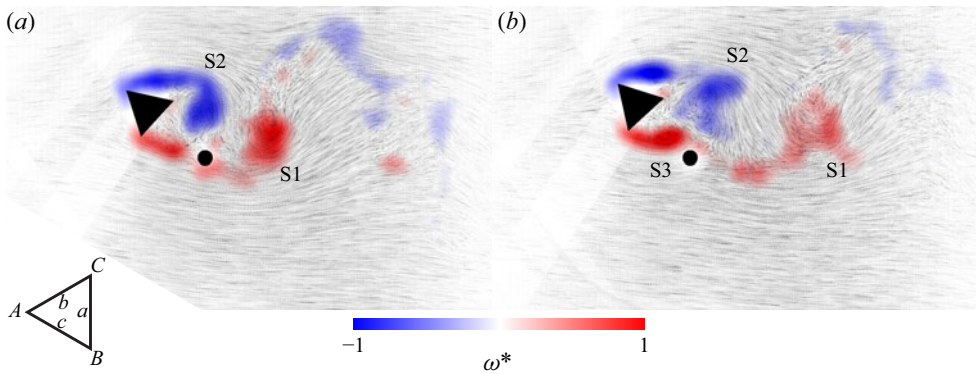

Figure 16. Snapshots of the wake for Case 2 in the convex orientation at $U^* = 14.1$. The maximum vorticity magnitude in these snapshots is $\omega = 59.3\,\text{s}^{-1}$.

with increasing reduced velocity in this region. Figure 16 shows the wake in this region of the response, which consists of a 2S vortex shedding pattern where in panel (*a*), the positive vortex S1 has been shed and is travelling downstream and the negative vortex S2 is shedding from edge *A*. In panel (*b*), S2 is moving downstream and S3 is just separating from edge *B*. Note that in this region, the shear layer forming from edge *A* never attaches to side *b*.
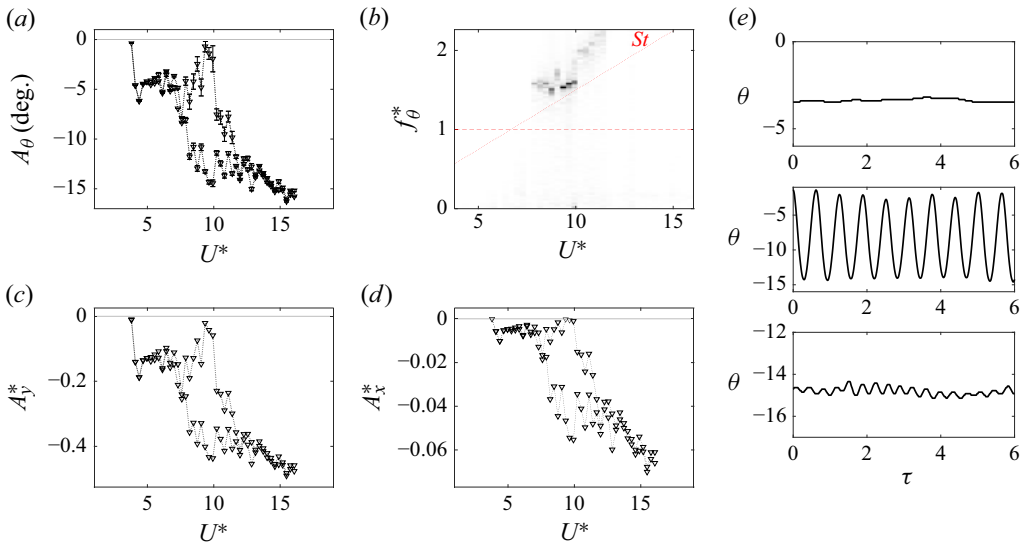
Figure 17. Case 3 in the concave orientation. (*a*) Angular amplitude of oscillations, (*b*) frequency contents of oscillations, (*c*) the amplitude of the cross-flow oscillations and (*d*) the amplitude of the inline oscillations. Panel (*e*) shows example time series at $U^* = 5.8$, $U^* = 9.6$ and $U^* = 14.9$ from top to bottom, respectively.

6. Case 3: when a side of the triangle is parallel to the flow

Here, the prism is oriented such that one side is parallel to the incoming flow. This completely breaks all symmetries in the system and, therefore, the resulting response for both the concave and the convex orientations will be asymmetric.

6.1. *In a concave orientation*

A series of very different behaviours are observed when one side of the prism is parallel with the flow at $\theta = 0°$ (figure 17). In the concave orientation, the incoming flow is deflected in the $+y$ direction as it contacts side b (see figure 18) and as a result, the prism is deflected in the $-y$ direction, causing a $-\theta$ rotation. The direction of the mean displacement causes the prism to rotate towards the neutral orientation similar to that observed in Case 2, where one edge of the prism was pointed upstream. This displacement arises from the fact that the majority of the incoming flow that interacts with the prism only interacts with one side, which, due to the asymmetric initial orientation, is angled and deflects the flow to one side. The reaction force then causes the prism to move in the opposite direction, until the flow force is balanced by the restoring force on the structure. Up until $U^* \approx 8$, the prism has a mean displacement of $\theta \approx 5°$ and exhibits no significant oscillations. As the reduced velocity is further increased however, oscillations begin at a frequency near the predicted Strouhal shedding frequency, which, at this reduced velocity, is ∼50 % higher than the natural frequency, as seen in figure 17(*b*). This region also corresponds to a linear increase in the mean displacement as the reduced velocity is increased, and this increase in the mean displacement continues even after the oscillations die off, at $U^* \approx 12$ (figure 17*a*).

Figure 18 shows snapshots of the wake for sample cases of $U^* = 9.9$, 13.1 and 15.2. At lower reduced velocities, shear layers roll up into vortices downstream at a distance of ∼2.5 times the side length of the prism, resulting in a 2S shedding pattern. As the reduced velocity is increased, the formation length shrinks and the 2S pattern becomes
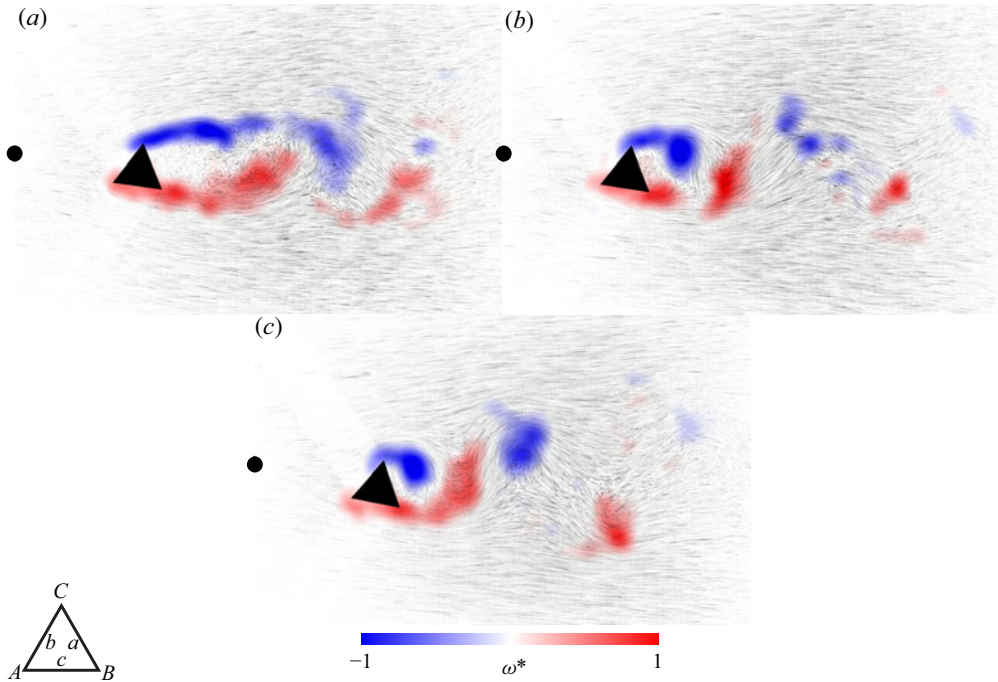
Figure 18. Snapshots of the wake for Case 3 in the concave orientation at (*a*) $U^* = 9.9$, (*b*) $U^* = 13.1$ and (*c*) $U^* = 15.2$. The maximum vorticity magnitudes in these snapshots are $\omega = 32.2\,\mathrm{s}^{-1}$, $\omega = 46.7\,\mathrm{s}^{-1}$ and $\omega = 55.7\,\mathrm{s}^{-1}$, respectively. A 2S shedding pattern is observed in the wake for all three reduced velocities. Video of the $U^* = 13.1$ example is shown in supplementary movie 5.

more pronounced, somewhat similar to the trend observed in Case 2, placed in the concave orientation discussed in §5.

6.2. *In a convex orientation*

In the convex orientation, the prism starts oscillating at a reduced velocity of $U^* \approx 4$. A summary of the response for this case is shown in figure 19, wherein four different regions of response can be observed. The waveform of the time histories also vary as the reduced velocity is increased. Samples of these waveforms are given in figure 20. In what follows, we discuss the details of the response in these four different regions.

6.2.1. *Region 1*

In the first region, from $U^* \approx 4$ to $U^* = 8.5$, the response is similar to that observed in the concave orientation, the prism is deflected asymmetrically away from the side that encounters the flow. However, unlike in the concave case, this motion causes the prism to rotate such that it is oriented similar to its initial condition in Case 1, where one side saw the flow first. The drag generated by this orientation of the prism relative to the flow causes the oscillations to be slightly biased in this direction initially, but as the reduced velocity is increased, the positive and negative amplitudes quickly become more comparable but the motion of the prism stays asymmetric (Region 1 in figure 19*a*). These oscillations begin at $U^* \approx 4$ with a very small amplitude and a frequency primarily at $\sim 50\,\%$ of the natural frequency, with some frequency contribution at the natural frequency as well (figure 19*b*). The amplitude of oscillations increases linearly with the reduced velocity in this region, as does the main frequency, which reaches $\sim 66\,\%$ of f_{nw} by $U^* = 8.5$ with
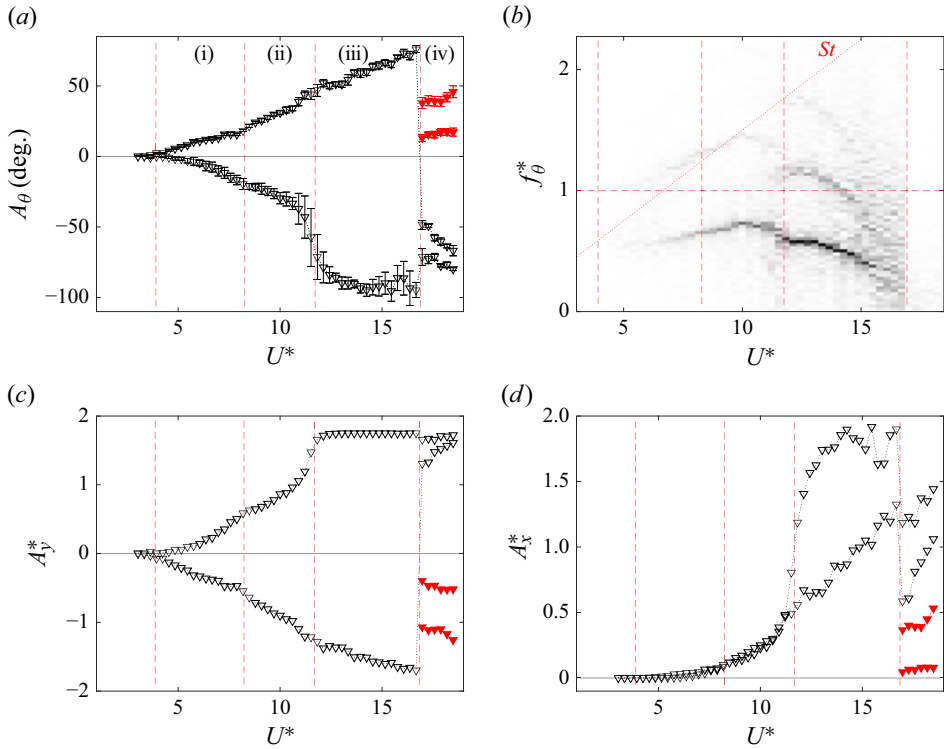
Figure 19. Case 3 in the convex orientation. (*a*) Angular amplitude of oscillations, (*b*) frequency contents of oscillations, (*c*) the cross-flow amplitude and (*d*) the inline amplitude of oscillations. The unfilled black markers represent the response of the prism as the reduced velocity is increased. The filled red markers represent a second stable response to which the prism converges, if disturbed far enough from the other stable solution.
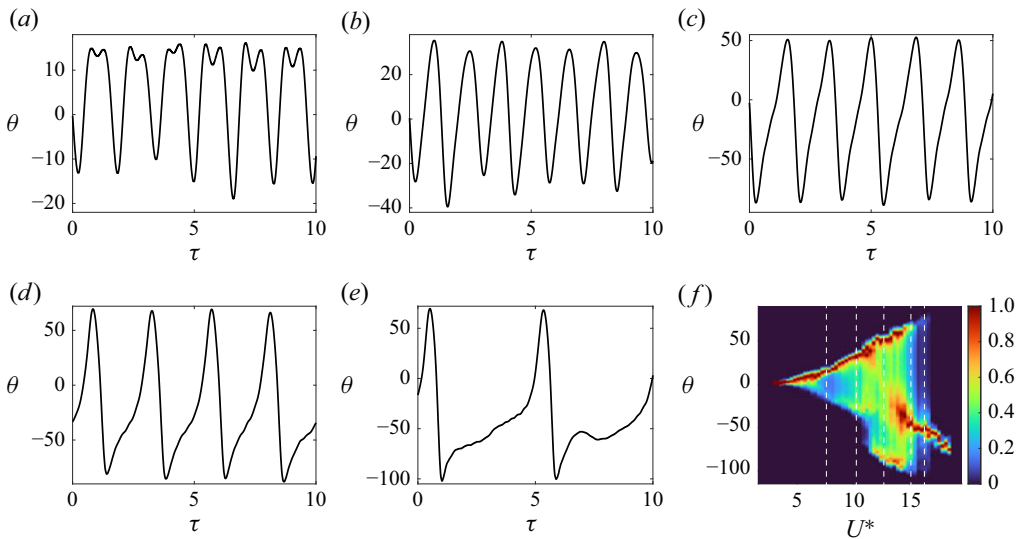

Figure 20. Sample time histories of the prism response at (*a*) $U^* = 7.6$, (*b*) $U^* = 10.3$, (*c*) $U^* = 12.7$, (*d*) $U^* = 14.5$ and (*e*) $U^* = 16.4$. Panel (*f*) shows the relative time the prism spends at each location as it oscillates. The vertical dotted lines in this panel show the locations of the time histories shown in panels (*a*)–(*e*).

the secondary frequency at $\sim 133\%$ of f_{nw}, maintaining the 2:1 ratio between the two for the entire region. The higher frequency component of the response occurs in phase with the lower frequency such that the positive peaks of the time history in this region exhibit a secondary, small-scale oscillation over what is otherwise a largely periodic behaviour (see figure 20*a*). The dwelling behaviour at the positive displacement, seen in this region, is caused by the in-phase second harmonic and appears as a dark red band along the maximum positive displacement in figure 20(*f*). This figure shows a histogram of the time histories of the prism at each reduced velocity, where the response is binned into 1 degree increments. The counts for each position are then normalised by the maximum count for that reduced velocity and the results are compiled into the heat map shown in the figure. This figure provides a measure of how the time histories for this case change with reduced velocity.

6.2.2. *Region 2*

The asymmetry in the time history disappears at $U^* \approx 8.8$, marking the beginning of the second region of the response. In this second region, oscillations are periodic as shown in figure 20(*b*), with a frequency that ranges from $\sim 66\%$ of f_{nw} at the beginning of this region to $\sim 75\%$ of f_{nw} at approximately $U^* = 10$, and then back to $\sim 66\%$ of f_{nw} by $U^* \approx 11.5$, at the end of this region (figure 20*b*).

In the wake snapshots of a sample case within Region 2 in figure 21, panel (*a*) shows that a negative vortex S1 is just shed from the prism (while the prism rotates CCW) and a positive vortex (S2) is forming around the downstream edge *B*. As the prism moves in the CCW direction, at $\theta \approx 0°$, this vortex is shed and the prism continues to move until it reaches its maximum CCW displacement as shown in panel (*b*). The prism then stays in this location long enough for two vortices, S3 and S4, to form and shed. As S4 is shed, the CCW torque on the prism is reduced enough that it begins moving CW, as shown in panel (*c*). Panel (*d*) shows the prism returning to its starting position, with S5 analogous to S1 from the previous cycle. Note that in this shedding pattern, the vortices shed in the wake are not necessarily synchronised with the oscillation frequency. Synchronisation exists only in a half-cycle of oscillations, but in the other half-cycle, the vortices are shed as the bluff body is almost stationary for a period of time.

6.2.3. *Region 3*

The onset of the third region is marked by a significant and sudden increase in the amplitude of response in the $-\theta$ direction, to approximately $-95°$. In this region, the amplitude in the $-\theta$ direction stays approximately the same, while the $+\theta$ amplitude increases linearly from $\sim 50°$ to $\sim 75°$ as the reduced velocity is increased to $U^* = 16.7$. Throughout this region, the time history becomes increasingly asymmetric. Initially, the time history's waveform becomes more saw-toothed as the motion from $-\theta$ displacement to $+\theta$ displacement occurs increasingly more slowly, compared with the return motion, as shown in figure 20(*c*). As the reduced velocity is increased, an especially slow region of travel appears at approximately $\theta = -50°$, when the prism is moving in the CCW direction. Figure 20(*d*) shows a sample time history in this region, where the prism travels rapidly from a maximum of $\sim 70°$ to approximately $-85°$, but takes nearly three and a half times as long to return.

The slow motion of the prism at approximately $\theta = -50°$ becomes increasingly elongated as the reduced velocity is increased further, developing into a distinct plateau in the response, until the time history takes on a heart-beat like waveform at the end of this region of the response, as shown in figure 20(*e*). The increasing duration the prism spends
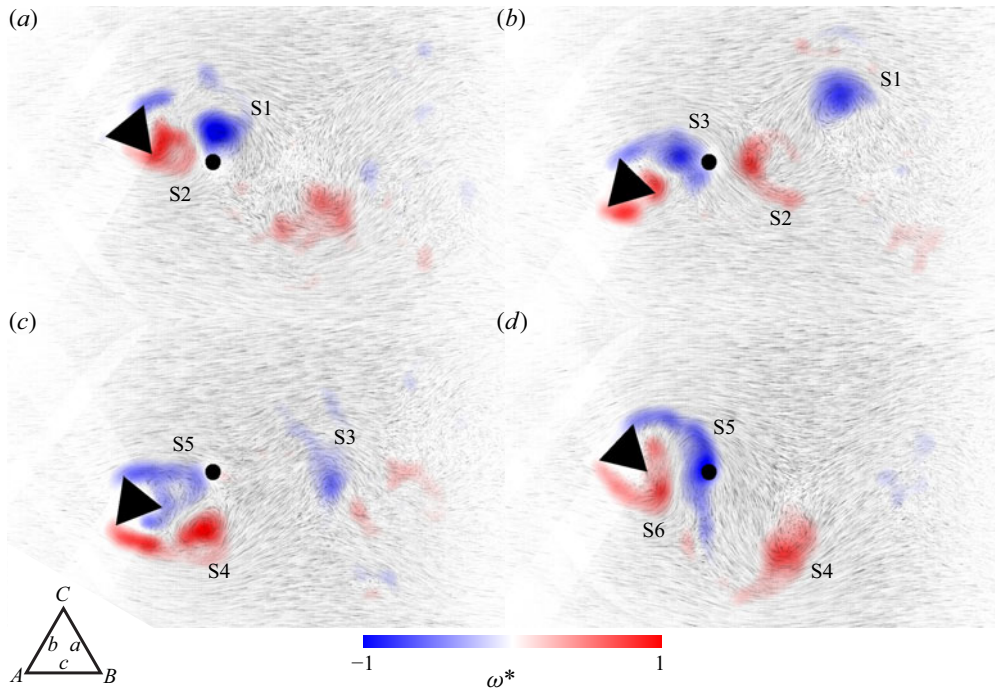
Figure 21. Snapshots of the wake for a sample case in Region 2 of Case 3 in the convex orientation at $U^* = 9.4$. The maximum vorticity magnitude in these snapshots is $\omega = 53.7\,\mathrm{s}^{-1}$.

at this approximately $-50°$ location is especially apparent in the positional mapping seen in figure 20(f). This behaviour is also noticeable in the frequency content of the response, which shows a primary frequency of $\sim 66\,\%$ of f_{nw} at the start of this region, with contributions at the second and third harmonics, that continuously decreases to a value of $\sim 33\,\%$ of f_{nw} before the frequencies diffuse at the end of the region. This broad spectrum of frequency content of the response arises from the increasing aperiodicity due to the increase in the duration the prism occupies this plateau at approximately $-50°$.

The wake that arises from this motion is shown in figure 22 for a sample case. In panel (a), the negative vortex S1 is just shed from edge C and another negative vortex, S2, is being formed around edge A. As S2 is shed, the prism begins moving counterclockwise and numerous single vortices are shed, alternating from edges B and C (S3–S8, panels b–e). As the prism approaches its maximum $+\theta$ displacement, vortex S9 is formed around edge A, and when shed, the prism rapidly begins moving back in the $-\theta$ direction. As the prism traverses the flow, a few weak vortices (S10–S12) are shed from edges A and B, as seen in panels (f) and (g). Meanwhile, a vortex begins forming around edge C, which stays attached to side a until the prism reaches its maximum displacement in the $-\theta$ direction, when this vortex is shed as vortex S13, as seen in panel (h).

6.2.4. *Region 4*

The last region of response for this case begins at $U^* = 16.7$, where the prism never escapes the slow region of travel and instead stays at approximately a mean displacement that increases linearly with reduced velocity from $\theta \approx -55°$ at the beginning of this
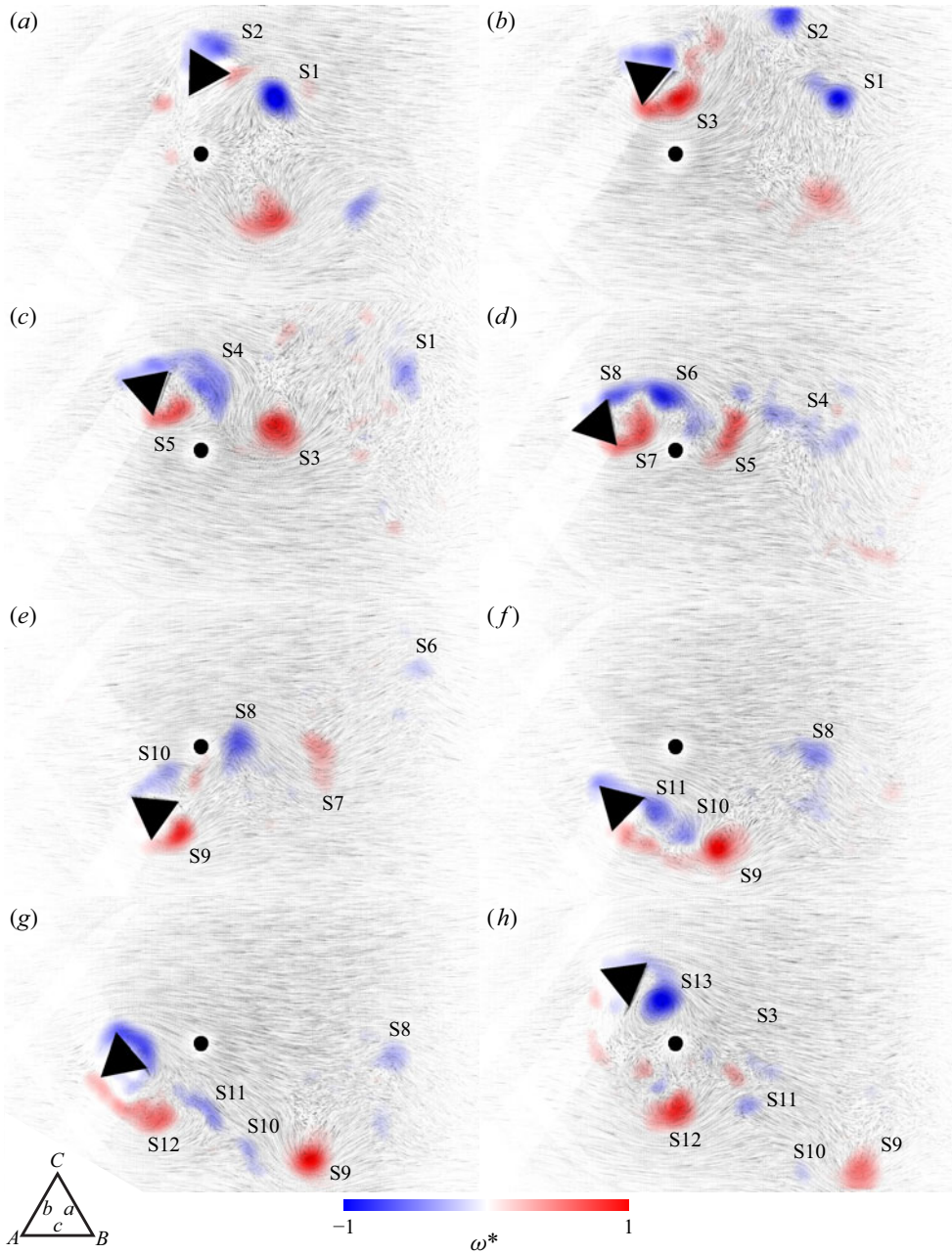
Figure 22. Snapshots of the wake for a sample case in Region 3 of Case 3 in the convex orientation at $U^* = 14.9$. The maximum vorticity magnitude in these snapshots is $\omega = 93.2\,\text{s}^{-1}$. Video of this example is shown in supplementary movie 6.

region to $\theta \approx -75°$ at the highest reduced velocity tested, $U^* = 18.5$. There is some small-amplitude turbulence-induced oscillations of the prism in this region, but the prism stays at this diverged location. In this region, the wake exhibits a 2S vortex shedding pattern.

While the negative mean displacement was observed in every trial, it was also discovered that there is another stable branch in the response. If, at reduced velocities
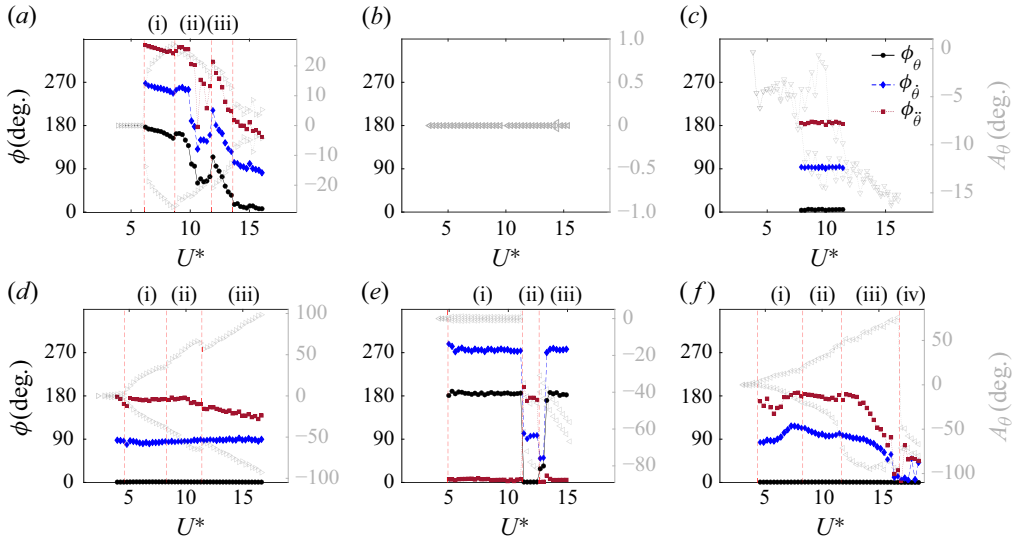
Figure 23. Phase difference between the flow-induced torque acting on the prism and the prism's displacement (black circles), velocity (blue diamonds) and acceleration (red squares) in the (*a*–*c*) concave orientation for (*a*) Case 1, (*b*) Case 2 and (*c*) Case 3, and in the (*d*–*f*) convex orientation for (*d*) Case 1, (*e*) Case 2 and (*f*) Case 3. Oscillation amplitudes are shown in grey. Vertical red dashed lines indicate the different regions of response where relevant.

of $U^* = 16.7$ or greater, the prism is manually positioned at $\theta \approx 30°$, it remains near this value, exhibiting similar behaviour to that observed in the $-\theta$ branch of the response. This alternate $+\theta$ branch is shown with the filled-in red markers in figure 19, but not shown in figure 20(*f*) as it does not occur without intervention.

7. Phasing between the flow-induced torque and the prism's displacements

By considering the phasing between the flow-induced torque and the prism's oscillations, we will shed light on the mechanism behind different responses of the prism observed for its different initial conditions.

Considering the concave orientation of Case 1 (figure 23*a*), at the onset of oscillations and throughout the first region of the response, the phasing of the first harmonic of the torque is $\phi \approx 180°$ relative to the displacement of the prism. This is despite the fact that this case exhibits a lock-in range, oscillation amplitudes and frequencies, and vortex shedding patterns very much similar to those observed in the cross-flow VIV of a cylinder. In the cylinder VIV case, however, the onset of oscillations, and the entire initial and upper branch of the response occur with a phase between force and displacement of $\phi \approx 0°$. Only for the lower branch of the lock-in range, a phase jump to $\phi \approx 180°$ is observed (Khalak & Williamson 1999). Here, in the concave orientation of Case 1, however, a phase shift occurs in the middle of region (ii), but instead of increasing, the phase drops to $\phi \approx 60°$, where it remains until the beginning of region (iii), where it jumps up to $\phi \approx 120°$, before decreasing steadily and reaching $\phi \approx 0°$ just as the lock-in range ends. The oscillations for this case are effectively sinusoidal across the entire lock-in range, and as a result, the phasing for the velocity and acceleration closely follow the same trends as the displacement phase, offset by $+90°$ and $+180°$, respectively, as expected.

For the convex orientation of Case 1 (figure 23*d*), as discussed in § 4.2, the frequency and amplitude responses are very similar to those observed by Seyed-Aghazadeh *et al.* (2015). This similarity holds true for the force phasing as well, although it should be noted that Seyed-Aghazadeh *et al.* (2015) report force/displacement phasing for an angle of attack that is rotated by 5° relative to the Case 1 orientation here. For both, the force phasing is near 0° relative to the displacement from the onset of oscillations up to the highest reduced velocities tested. Here, we observe an interesting trend in the acceleration phasing, which is steady at $\phi \approx 180°$ in the first region, corresponding to the VIV response, and then begins to decrease in region (ii), the transition region, ultimately reaching a minimum value of $\phi \approx 120°$ by the end of region (iii). This trend is the result of the fact that the displacement time series becomes increasingly less sinusoidal in this region and looks more like a shark fin at these higher reduced velocities.

In Case 2, the prsim in the concave orientation does not oscillate and therefore, there is no phase to be calculated (figure 23*b*). The prism in the convex orientation, however, does oscillate and gives rise to some interesting observations (figure 23*e*). In region (i) of the response, there are small-amplitude oscillations whose frequency follows the Strouhal law, and therefore, are not considered VIV. In this region, the forces on the prism are completely out of phase with the displacement. When the prism diverges in region (ii) and begins oscillating about a non-zero mean displacement, the phasing drops to $\phi \approx 0°$. This is then followed by region (iii), where the oscillation amplitude drops and the phasing returns to $\phi \approx 180°$. This gives the post-divergence response of this case the appearance, in amplitude and phasing at least, of the canonical cross-flow VIV case, where the jump in phasing corresponds to a reduction in amplitude as the lock-in range switches from the upper branch to the lower branch. This is in spite of the fact that only half of an oscillation cycle behaves as a VIV response, as discussed in § 5.2.

For Case 3, the concave orientation exhibits a near 0° phase for all reduced velocities that cause any significant oscillations (figure 23*c*). Meanwhile, the convex orientation (figure 23*f*) follows the 'combined VIV-galloping' trend seen in the convex orientation of Case 1 and noted by Seyed-Aghazadeh *et al.* (2017) for the 1-DOF cross-flow case. As with Case 1, the convex orientation for Case 3 has $\phi \approx 0°$ for the displacement for all reduced velocities tested, and the velocity and acceleration phases are $\phi \approx 90°$ and $\phi \approx 180°$ respectively for the first two regions of the response, with some variations in region (i). As in Case 1, in region (iii), the acceleration phase decreases, however, here it drops all the way to $\phi \approx 0°$, before jumping up to $\phi \approx 50°$ in region (iv).

Collectively, the torque phasing data lead to two main conclusions. First, torque phasing of $\phi \approx 0°$ relative to displacement appears to be a requirement for, although not a guarantee of, galloping, as the convex orientations of Cases 1 and 3, and region (ii) of Case 2 in the convex orientation all exhibit this phasing with large-amplitude low-frequency oscillations. Second, oscillations at the shedding frequency predicted by the Strouhal law, as observed in region (i) of the concave orientation of Case 1, and regions (i) and (iii) of the convex orientation of Case 2 occur with $\phi \approx 180°$.

To further investigate the mechanism that causes the different flow-induced responses observed in these experiments, we decompose the flow-induced torque acting on the prism into the vortex torque and the potential flow added-mass torque using the method introduced by Lighthill (1986), and widely used and expanded upon by others, e.g. by Govardhan & Williamson (2000) and Zhao *et al.* (2014*b*) for forces in the transverse direction. Here, we extend this idea to torques that act on the prism. It has been shown that when the dominant frequency of the vortex component is at a 1 : 1 ratio with the displacement, it is the formation and shedding of vortices that drives the structural oscillations. Any jump in this frequency to higher ratios (2 : 1, 3 : 1, etc.) indicates that
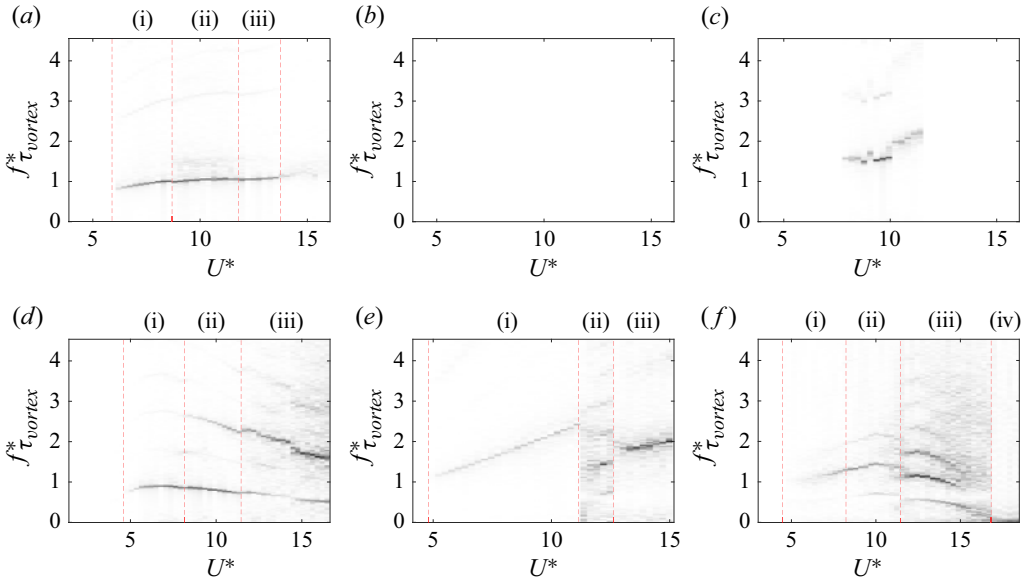
Figure 24. Vortex torque (τ_{vortex}) frequencies, normalised by the prism natural frequency in the (a–c) concave orientation for (a) Case 1, (b) Case 2 and (c) Case 3 and in the (d–f) convex orientation for (d) Case 1, (e) Case 2 and (f) Case 3.

the vortex shedding is no longer the primary driver of oscillations indicating a switch from VIV to galloping regimes (Seyed-Aghazadeh *et al.* 2017). To determine the influence of vortices on the prism, we calculate the vortex torque, τ_{vortex}, as

$$\tau_{vortex} = \tau_{total} - \tau_{potential}, \tag{7.1}$$

where τ_{total} is from the left-hand side of (2.1) and $\tau_{potential}$, adapted from Govardhan & Williamson (2000), is defined as

$$\tau_{potential} = -I_{am}\ddot{\theta}, \tag{7.2}$$

with I_{am} being the inertial effect due to the added mass. This is calculated using an added mass coefficient of $C_{am} = 1.53$, derived experimentally for an equilateral triangular prism by Goldschmidt & Protos (1968).

Figure 24 shows the frequency response for τ_{vortex} for all cases in both orientations. Panel (a) shows the response for Case 1 in the concave orientation, and while there is a small contribution form the third harmonic, the vast majority of the harmonic content is in a $1:1$ ratio with the displacement frequency shown in figure 4(b). This is in contrast to the convex orientation for this case shown in panel (d), where an increasing contribution of the third harmonic is apparent in the transitional region (ii), which becomes the dominant frequency in the galloping observed in region (iii). The translational oscillation case discussed by Seyed-Aghazadeh *et al.* (2017) shows similar transitional and galloping regimes corresponding to a shift to higher frequencies by the vortex force. The question then arises as to why the concave orientation allows the vortex torque to continue influencing the motion into the higher reduced velocities. By considering the snapshots of the wake shown in figure 7, it is apparent that as the prism approaches its maximum displacement, the afterbody of the prism is rotated such that it is in closer proximity to the other shear layer, and it appears that this physical proximity allows the influence of the vortex formation and shedding to persist for this orientation.

For Case 2 in the convex orientation (figure 24*e*), the vortex torque is at 1 : 1 ratio with displacement in region (i), switching to a 2 : 1 ratio, with notable contributions at other harmonics, in region (ii) once the prism diverges and begins low frequency oscillations about a non-zero mean value of θ, indicating a cessation of VIV as the divergence occurs. Then, in region (iii), as the oscillation amplitude decreases and the frequency increases, the 1 : 1 ratio is resumed.

For Case 3, shown in figure 24(*c,f*), the small amplitude oscillations observed in the concave orientation occur at a 1 : 1 ratio with the vortex torque, and while this indicates that it is the formation and shedding of vortices that is driving the motion, the lack of lock-in between the prism natural frequency and the shedding indicates that this is not a VIV response. In the convex orientation, the vortex torque frequency is twice that of the oscillation frequency for all reduced velocities, demonstrating that this is a galloping response for all regions up until divergence occurs in region (iv).

8. Conclusions

We have discussed the results of a series of experiments performed to investigate the response of an equilateral triangular prism confined to travel on a curved path and placed in fluid flow. This is a curious case, because if the structure oscillates, as we have shown it does, the relative angle of attack that it makes with the incoming flow changes continuously throughout its oscillations. The expected oscillations of the structure in this case are in both the IL and CF directions, while the system is still a 1-DOF system. The question that we raised and investigated in this work was how would a bluff body with a non-circular cross-section (a triangular cross-section for this specific case) respond to an increasing incoming flow when its motion is restricted to a curved path and how would this response depend on the initial conditions. We have shown in our results that the initial condition, i.e. the position of the triangular prism at the beginning of these experiments, has a significant influence on the response. While we expected some influence of this initial condition on the response, due to the fact that the system is a highly nonlinear one, the extent of dependency on the initial conditions that we have observed is beyond our original expectation.

We considered three different initial angles of attack for the prism: in Case 1, a flat side of the prism saw the flow first; in Case 2, an edge of the prism saw the flow first, and in Case 3, one side of the prism was parallel to the flow. Each of these cases were tested with both a concave and a convex configuration relative to the incoming flow, where in the concave configuration, the prism was allowed to oscillate about a fixed point located upstream of the prism, and in the convex configuration, about a fixed point downstream of the prism. The radius of this path was 1.75 times the side length of the prism, a distance that was chosen because in our previous work considering a cylinder in similar configurations, this radius corresponded to the maximum amplitude of oscillations that we observed.

Case 1 exhibits responses akin to those previously observed for FIV of a bluff body on a linear path, namely VIV, in the concave configuration, and galloping, in the convex configuration. Unlike the translational oscillation case that results in a galloping response for a triangular prism at this initial angle of attack however, the concave orientation only exhibits a VIV response, and an analysis of the decomposed fluid torques acting on the prism reveals that the influence of vortex shedding on the structure persists throughout the range of reduced velocities, and the proximity of the prism afterbody to the shear layers is proposed as the mechanism that causes this behaviour. For the concave configuration, the wake consists of a 2S shedding over the majority of the reduced velocities tested, but at the largest amplitudes of oscillations, a 2C pattern is observed in the wake. In the convex

orientation, an initial region of VIV response exhibits 2P shedding, which transitions to 2P + 2S shedding as the response transitions to a galloping behaviour. Once galloping is fully developed, multiple vortices are shed in each cycle of oscillations, as expected in a galloping response.

In Case 2, where one edge encounters the flow first, no oscillations are observed in the concave orientation. This matches previously observed results considering this angle of attack when the prism is allowed to move on a linear CF path. In this case, the wake is characterised by long shear layers that roll up into 2S vortices far downstream of the prism at higher reduced velocities and therefore do not cause oscillations. In the convex orientation, at lower reduced velocities, no oscillations are observed. However, above a critical reduced velocity, the mean drag force causes a large mean deflection of the prism, which creates a new mean angle of attack, and oscillations with an asymmetric waveform begin. These oscillations result in the shedding of a large number of vortices in each cycle. At higher reduced velocities, the amplitude of oscillations drops and the wake returns to a 2S pattern.

Case 3 in the concave orientation has minimal oscillations throughout the reduced velocity range tested, but there is a steady increase in the static deflection as the reduced velocity is increased. The convex orientation for this case exhibits the most complex response of all six configurations. Initially, at lower reduced velocities, there is a VIV-like response that quickly transitions into an increasingly asymmetric waveform. In the wake of these asymmetric oscillations, the vortices are shed synchronously with oscillations in one half-cycle – similar to what is observed in a VIV response – and asynchronously in the other half-cycle – similar to what is observed in a galloping response. The frequency of oscillations continuously decreases, and increasingly more single vortices are shed during the half-cycle that resembles a galloping response. This decrease in the oscillation frequency is the result of a widening plateau in the time history, at approximately $\theta = -50°$, where the prism dwells while travelling in the CCW direction. Eventually, the duration of this plateau grows to the extent that the prism stays at that position and undergoes only turbulence-induced oscillations, while the wake simplifies to a 2S shedding pattern. In this region, two stable static responses are observed, the second one at an angle of approximately $\theta = 30°$.

Overall, the system exhibits a myriad of responses depending on its initial condition and orientation: from typical VIV and galloping responses to asymmetric galloping, a response that resembles a combination of VIV and galloping behaviour, and simply static divergence. The phasing of the flow-induced torque relative to the prism displacement exhibits distinct values corresponding to these responses. When galloping is observed, the torque and the displacement are in phase, and when VIV is observed, they are out of phase. The different structural responses in turn result in different patterns in the wake of the prism: vortex shedding synchronised with the observed oscillations in the form of 2S, 2P or 2C patterns as well as asynchronous shedding in the wake of the galloping responses, and wakes that resemble a combination of VIV wakes (where shedding is synchronised with oscillations) and galloping wakes (where the shedding is independent from the oscillation frequency).

Although this is only a 1-DOF system, due to its two unique features, a non-circular cross-section and a curved path, it exhibits very rich dynamics. The variable angle of attack within one cycle of oscillations, and the combined influence of components of the lift and drag forces in the direction of motion are the key reasons for observing these complex behaviours.

Supplementary movies. Supplementary movies are available at https://doi.org/10.1017/jfm.2025.10781.

Declaration of interests. The authors report no conflict of interest.

REFERENCES

ALAWADHI, E.M. 2013 Numerical simulation of fluid flow past an oscillating triangular cylinder in a channel. *J. Fluid Engng* **135** (4), 041202.

ALONSO, G. & MESEGUER, J. 2006 A parametric study of the galloping stability of two-dimensional triangular cross-section bodies. *J. Wind Engng* **94**, 241–253.

ALONSO, G., MESEGUER, J. & PÉREZ-GRANDE, I. 2005 Galloping instabilities of two-dimensional triangular cross-section bodies. *Exp. Fluids* **38** (6), 789–795.

ARIONFARD, H. & MOHAMMADI, S. 2021 Numerical investigation of the geometrical effect on flow-induced vibration performance of pivoted bodies. *Energies* **14** (4), 1128.

ARIONFARD, H. & NISHI, Y. 2017 Experimental investigation of a drag assisted vortex-induced vibration energy converter. *J. Fluids Struct.* **68**, 48–57.

BAO, Y., ZHOU, D. & ZHAO, Y. 2010 A two-step Taylor-characteristic-based Galerkin method for incompressible flows and its application to flow over triangular cylinder with different incidence angles. *Intl J. Numer. Meth. Fluids* **62** (11), 1181–1208.

BARRERO-GIL, A., ALONSO, G. & SANZ-ANDRES, A. 2010 Energy harvesting from transverse galloping. *J. Sound Vib.* **329** (14), 2873–2883.

BEARMAN, P.W. 1984 Vortex shedding from oscillating bluff bodies. *Annu. Rev. Fluid Mech.* **16**, 195–222.

BENNER, B.M., CARLETON, A.G. & MODARRES-SADEGHI, Y. 2025 Transition from vortex-induced vibrations to galloping in a flexible square prism. *J. Fluid Mech.* **1007**, A76.

BENNER, B.M. & MODARRES-SADEGHI, Y. 2021 Vortex-induced vibrations of a one-degree-of-freedom cylinder transitioning from the inline to the crossflow degree of freedom. *Phys. Rev. Fluids* **6**, 114702.

BERNITSAS, M.M., RAGHAVAN, K., BEN-SIMON, Y. & GARCIA, E.M.H. 2008 VIVACE (vortex induced vibration aquatic clean energy): a new concept in generation of clean and renewable energy from fluid flow. *J. Offshore Mech. Arctic Engng* **130** (4), 041101

BLEVINS, R.D. 1990 *Flow-Induced Vibrations*. Nostrand Reinhold Co.

BOKAIAN, A. & GEOOLA, F. 1984 Wake-induced galloping of two interfering circular cylinders. *J. Fluid Mech.* **146**, 383–415.

BOURGUET, R. 2023 Flow-induced vibrations of a cylinder along a circular arc. *J. Fluid Mech.* **954**, A7.

BOURGUET, R. & JACONO, D.L. 2014 Flow-induced vibrations of a rotating cylinder. *J. Fluid Mech.* **740**, 342–380.

BOURGUET, R., MODARRES-SADEGHI, Y., KARNIADAKIS, G.E. & TRIANTAFYLLOU, M.S. 2011 Wake-body resonance of long flexible structures is dominated by counterclockwise orbits. *Phys. Rev. Lett.* **107** (13), 134502.

CAGNEY, N. & BALABANI, S. 2013*a* Mode competition in streamwise-only vortex induced vibrations. *J. Fluids Struct.* **41**, 156–165.

CAGNEY, N. & BALABANI, S. 2013*b* Wake modes of a cylinder undergoing free streamwise vortex-induced vibrations. *J. Fluids Struct.* **38**, 127–145.

CARLETON, A. & MODARRES-SADEGHI, Y. 2024 Angular vortex-induced vibrations of a cylinder. *J. Fluids Struct.* **126**, 104087.

CARLSON, D.W., CURRIER, T.M. & MODARRES-SADEGHI, Y. 2021 Flow-induced vibrations of a square prism free to oscillate in the cross-flow and inline directions. *J. Fluid Mech.* **919**, A2.

CUI, Z., ZHAO, M., TENG, B. & CHENG, L. 2015 Two-dimensional numerical study of vortex-induced vibration and galloping of square and rectangular cylinders in steady flow. *Ocean Engng* **106**, 189–206.

DAHL, J.M., HOVER, F.S. & TRIANTAFYLLOU, M.S. 2007 Resonant vibrations of bluff bodies cause multivortex shedding and high frequency forces. *Phys. Rev. Lett.* **99**, 144503.

DAHL, J.M., HOVER, F.S., TRIANTAFYLLOU, M.S. & OAKLEY, O.H. 2010 Dual resonance in vortex-induced vibrations at subcritical and supercritical Reynolds numbers. *J. Fluid Mech.* **643**, 395–424.

DE, A.K. & DALAL, A. 2007 Numerical study of laminar forced convection fluid flow and heat transfer from a triangular cylinder placed in a channel. *J. Heat Transfer* **129**, 646–656.

DENIZ, S. & STAUBLI, T. 1997 Oscillating rectangular and octagonal profiles: interaction of leading-and trailing-edge vortex formation. *J. Fluids Struct.* **11** (1), 3–31.

EDRAKI, M., BENNER, B. & MODARRES-SADEGHI, Y. 2023 Energy extraction from galloping of a prism restricted to oscillate at a fixed magnitude. *J. Fluids Struct.* **118**, 103840.

GOLDSCHMIDT, V.W. & PROTOS, A. 1968 Added mass of equilateral-triangular cylinders. *J. Engng Mech. Div.* **94** (6), 1539–1546.

GOVARDHAN, R. & WILLIAMSON, C.H.K. 2000 Modes of vortex formation and frequency response of a freely vibrating cylinder. *J. Fluid Mech.* **420**, 85–130.

GURIAN, T.D., CURRIER, T. & MODARRES-SADEGHI, Y. 2019 Flow force measurements and the wake transition in purely inline vortex-induced vibration of a circular cylinder. *Phys. Rev. Fluids* **4** (3), 034701.

GURIAN, T.D. & MODARRES-SADEGHI, Y. 2021 Vortex-induced vibrations of a square prism free to oscillate in the inline direction. *J. Fluids Struct.* **102**, 103237.

JAFARI, M., HOU, F. & ABDELKEFI, A. 2020 Wind-induced vibration of structural cables. *Nonlinear Dyn.* **100**, 351–421.

KHALAK, A. & WILLIAMSON, C.H.K. 1999 Motions, forces and mode transitions in vortex-induced vibrations at low mass-damping. *J. Fluids Struct.* **13** (7–8), 813–851.

KUMAR DE, A. & DALAL, A. 2006 Numerical simulation of unconfined flow past a triangular cylinder. *Intl J. Numer. Meth. Fluids* **52**, 801–821.

LIGHTHILL, J. 1986 Fundamentals concerning wave loading on offshore structures. *J. Fluid Mech.* **173**, 667–681.

MA, X. & ZHOU, S. 2022 A review of flow-induced vibration energy harvesters. *Energy Convers. Manage.* **254**, 115223.

MALEFAKI, I. & KONSTANTINIDIS, E. 2020 Assessment of a hydrokinetic energy converter based on vortex-induced angular oscillations of a cylinder. *Energies* **13** (3), 717.

MODARRES-SADEGHI, Y. 2022 *Introduction to Fluid-Structure Interactions*. Springer Nature.

NAUDASCHER, E. & WANG, Y. 1993 Flow-induced vibrations of prismatic bodies and grids of prisms. *J. Fluids Struct.* **7** (4), 341–373.

NEMES, A., ZHAO, J., LO JACONO, D. & SHERIDAN, J. 2012 The interaction between flow-induced vibration mechanisms of a square cylinder with varying angles of attack. *J. Fluid Mech.* **710**, 102–130.

OBASAJU, E.D., ERMSHAUS, R. & NAUDASCHER, E. 1990 Vortex-induced streamwise oscillations of a square-section cylinder in a uniform stream. *J. Fluid Mech.* **213**, 171–189.

PAÏDOUSSIS, M.P., PRICE, S.J. & DE LANGRE, E. 2010 *Fluid-Structure Interactions: Cross-Flow-Induced Instabilities*. Cambridge University Press.

PARKINSON, G. & SMITH, J. 1964 The square prism as an aeroelastic non-linear oscillator. *Q. J. Mech. Appl. Maths* **17**, 225–239.

PARKINSON, G. & WAWZONEK, W. 1981 Some considerations of combined effects of galloping and vortex resonance. *J. Wind Engng Ind. Aerodyn.* **8**, 135–143.

SARPKAYA, T. 2004 A critical review of the intrinsic nature of vortex-induced vibrations. *J. Fluids Struct.* **19**, 389–447.

SEYED-AGHAZADEH, B., CARLSON, D.W. & MODARRES-SADEGHI, Y. 2015 The influence of taper ratio on vortex-induced vibration of tapered cylinders in the crossflow direction. *J. Fluids Struct.* **53**, 84–95.

SEYED-AGHAZADEH, B., CARLSON, D.W. & MODARRES-SADEGHI, Y. 2017 Vortex-induced vibration and galloping of prisms with triangular cross-sections. *J. Fluid Mech.* **817**, 590–618.

SEYED-AGHAZADEH, B., EDRAKI, M. & MODARRES-SADEGHI, Y. 2019 Effects of boundary conditions on vortex-induced vibration of a fully submerged flexible cylinder. *Exp. Fluids* **60** (3), 38.

SEYED-AGHAZADEH, B. & MODARRES-SADEGHI, Y. 2016 Reconstructing the vortex-induced-vibration response of flexible cylinders using limited localized measurement points. *J. Fluids Struct.* **65**, 433–446.

SRIGRAROM, S. & KOH, A.K.G. 2008 Flow field of self-excited rotationally oscillating equilateral triangular cylinder. *J. Fluids Struct.* **24**, 750–755.

SU, Z., YU, L., HONGJUN, Z. & DONGFEI, Z. 2007 Numerical simulation of vortex-induced vibration of a square cylinder. *J. Mech. Sci. Technol.* **21** (9), 1415–1424.

SUNG, H.G., BAEK, H., HONG, S. & CHOI, J.-S. 2015 Numerical study of vortex-induced vibration of pivoted cylinders. *Ocean Engng* **93**, 98–106.

THIELICKE, W. & SONNTAG, R. 2021 Particle image velocimetry for MATLAB: accuracy and enhanced algorithms in PIVlab. *J. Open Res. Softw.* **9** (1).

TU, J., ZHOU, D., BAO, Y., HAN, Z. & LI, R. 2014 Flow characteristics and flow-induced forces of a stationary and rotating triangular cylinder with different incidence angles at low Reynolds numbers. *J. Fluids Engng* **45**, 107–123.

VANDIVER, J.K. 2012 Damping parameters for flow-induced vibration. *J. Fluids Struct.* **35**, 105–119.

WANG, S., ZHU, L., ZHANG, X. & HE, G. 2011 Flow past two freely rotatable triangular cylinders in tandem arrangement. *J. Fluids Engng* **133**, 081202.

WILLIAMSON, C.H.K. & GOVARDHAN, R. 2004 Vortex-induced vibrations. *Annu. Rev. Fluid Mech.* **36**, 413–455.

ZHAO, J., LEONTINI, J.S., LO JACONO, D. & SHERIDAN, J. 2014*a* Fluid-structure interaction of a square cylinder at different angles of attack. *J. Fluid Mech.* **747**, 688–721.

ZHAO, J., LEONTINI, J S., LO JACONO, D. & SHERIDAN, J. 2014*b* Fluid–structure interaction of a square cylinder at different angles of attack. *J. Fluid Mech.* **747**, 688–721.

ZHAO, M., CHENG, L. & ZHOU, T. 2013 Numerical simulation of vortex-induced vibration of a square cylinder at a low Reynolds number. *Phys. Fluids* **25** (2), 023603.

ZHU, H.B., PING, H., WANG, R., BAO, Y., ZHOU, D. & HAN, Z.L. 2019 Flow-induced vibration of a flexible triangular cable at low Reynolds numbers. *Phys. Fluids* **31** (5), 057101.